energies

MDPI

Article

Physics-Based Modelling of Plate-Fin Heat Exchangers

Mattia Grespan [1,*], Adriano Leonforte [1], Luigi Calò [1,2], Marco Cavazzuti [1] and Diego Angeli [1,3,*]

[1] DISMI – Dipartimento di Scienze e Metodi dell'Ingegneria, Università di Modena e Reggio Emilia, Via Amendola 2, Pad. Buccola, 42122 Reggio Emilia, Italy; adriano.leonforte@unimore.it (A.L.); marco.cavazzuti@unimore.it (M.C.)
[2] VEMA Industries S.r.l., Via Guido Rossa 8, 43058 Sorbolo-Mezzani, Italy; luigi.calo@vema-industries.com
[3] Centro Interdipartimentale EN&TECH, Piazzale Europa 1, 42124 Reggio Emilia, Italy
* Correspondence: mattia.grespan@unimore.it (M.G.); diego.angeli@unimore.it (D.A.)

Abstract: Aluminium plate-fin heat exchangers are widely used in automotive, aerospace, and other industrial applications. Extensive research has been conducted on these coolers, yet accurate predictive tools for their thermo-hydraulic performance are still lacking, due to the wide variety of geometric parameters and working fluids involved. This work proposes an original approach based purely on physical principles and established models, combining detailed numerical models for the extended surfaces and manifolds, with global models aimed at accurately evaluating overall head losses and heat transfer rates in plate-fin heat exchangers. Extended surfaces are studied by means of computational models of unitary fin modules under fully developed flow conditions. Entrance effects are analysed through dedicated numerical models. Numerical results on extended surfaces are extended to whole heat exchangers by global models for heat transfer and head losses, based on the $\varepsilon - \mathrm{NTU}$ method and the Darcy–Weisbach equation, respectively. The proposed approach is presented and validated through the analysis of a case study comprising several heat exchangers featuring different geometries and working fluids. Numerically derived heat transfer rates and head losses are compared with experimental data showing maximum deviations of $\pm 20\%$ for most of the tested configurations, highlighting the strength of the proposed modelling methodology.

Keywords: plate and fin heat exchanger; offset-strip fins; wavy fins; CFD; correlations; multiscale approach

check for updates

Academic Editors: Fabio Bozzoli and Marcelo José Colaço

Received: 11 December 2024
Revised: 12 January 2025
Accepted: 17 January 2025
Published: 22 January 2025

Citation: Grespan, M.; Leonforte, A.; Calò, L.; Cavazzuti, M.; Angeli, D. Physics-Based Modelling of Plate-Fin Heat Exchangers. *Energies* **2025**, *18*, 495. https://doi.org/10.3390/en18030495

Copyright: © 2025 by the authors. Licensee MDPI, Basel, Switzerland. This article is an open access article distributed under the terms and conditions of the Creative Commons Attribution (CC BY) license (https://creativecommons.org/licenses/by/4.0/).

1. Introduction

1.1. Motivations and Aims

Aluminium Plate-Fin Heat Exchangers (PFHEs), also referred to as plate and bar heat exchangers, are widely used in the automotive, agricultural, and power generation industries, where reliability is key. The stacked assembly of finned plates and side bars endow these heat exchangers with remarkable mechanical resistance and heat transfer properties. In spite of their widespread diffusion, both the design and verification processes of PFHEs still rely largely on rules of thumb and expensive testing campaigns. With the advent of the recent and repeated energy and financial crises, it is crucial for manufacturers to adopt suitable prediction tools in order to reduce the need for experimental tests and, in turn, contain design costs. Nevertheless, such tools must ensure a satisfactory accuracy in the estimation of both fluid dynamic and heat transfer performance, while maintaining a high degree of generality. However, most of the available models are based on parameter identification from experimental tests and, as such, suffer from two major drawbacks:

(i) the generality of these models is quite limited; (ii) the number of tests required to achieve reliable predictions is still high.

In this work, a simple but accurate numerical methodology is presented, aimed at the prediction of overall head losses and heat transfer rates in PFHEs. To maintain a high degree of generality, the present methodology is developed considering only nominal geometric parameters, physical principles, and established models, without resorting to the identification of any empirical parameter.

1.2. Literature Survey

Extended surfaces are a key component of any heat exchanger, as they allow for a substantial enhancement of heat transfer effectiveness compared to standard rectangular channels. The most commonly used extended surfaces in plate-fin exchangers often feature offset-strip and wavy or corrugated geometries. Offset-Strip Fins (OSFs) are characterized by high compactness, and their outstanding heat transfer performance is achieved though periodic interruptions of the boundary layers and the oscillating flow patterns present in the wakes of the fins. Over the years, OSFs have been the subject of several studies based on both experimental and numerical methods. Kays and London [1] and London and Shah [2] first provided a large set of experimental results on actual fin cores. Many authors, including Wieting [3], Mochizuki et al. [4], Manglik and Bergles [5], and Dubrovsky et al. [6], proposed empirical correlations for the evaluation of friction losses and heat transfer effectiveness in OSFs, which are based on the regression analysis of experimental results. Joshi and Webb [7] presented an analytical model for the laminar flow regime and a semi empirical approach for the turbulent one. All the aforementioned correlations were presented in terms of Colburn factor and Fanning friction factor, as a function of Reynolds and Prandtl numbers, and dimensionless geometric parameters. Numerical methods, improved by the rapid growth of computational capabilities over the last few decades, have been largely exploited to investigate the thermal performance of OSFs at a reduced cost. Recent studies employed 3D simulations with the standard Finite Volume approach and several turbulence models [8–10], while the Lattice Boltzmann method is employed for the study of extended surfaces in micro heat exchangers [11]. Kim et al. [12] investigated the effect of the turbulence model on numerical results, including the k-ω, the standard k-ε, the realizable k-ε, and the k-ω SST. The authors showed that numerical results obtained by means of the k-ω SST turbulence model are the ones in better agreement with the experimental results presented in [5].

Wavy Fins (WFs) are also used extensively in plate-fin heat exchangers, due to their superior resistance to clogging [13] in harsh environments, compared to offset-strip fins. The improvement in the thermo-hydraulic performance of wavy fins compared to plain ones is given by two main factors: at low Reynolds numbers ($\mathrm{Re} < 100$) the dominant effect is that of an increased effective flow length, while at high Re-values the onset of streamwise and spanwise counter rotating lateral vortices in the troughs of the fins lead to higher momentum transfer, along with a thinning of the thermal boundary layer [14]. The geometry of wavy fins is defined on the basis of the fin pitch, x, fin height, y, wave length, $2l$, fin thickness, t, and wave amplitude, a. In most of the studies concerning wavy fins, the performances are expressed in terms of isothermal Fanning friction factor and Colburn factor, as a function of the Reynolds number and of the three dimensionless parameters: aspect ratio, fin spacing ratio, and corrugation ratio. Several studies have addressed the thermo-hydraulic characterization of wavy fins either experimentally or numerically. The earliest experimental data can be found in [1] for three different geometries using air as the working fluid. Goldstein and Sparrow [15] studied corrugated channels with triangular waves by carrying out experiments based on the naphthalene sublimation

method. Rush et al. [16] conducted flow visualization tests to investigate fluid behaviour in the laminar and transitional flow regions. More recent experimental studies are found in [13,17]. Compared to experimental studies, numerical research on wavy fins is much sparser. Asako and Faghri [18] numerically investigated two-dimensional steady laminar flow in plate channels with triangular-profiled wall corrugations. Zhang et al. [19] and Metwally and Manglik [20] investigated two-dimensional laminar periodic flow in sinusoidal wavy channels with different corrugation angles and fin spacing values. Three-dimensional computational studies include those of Aliabadi et al. [21], Wen et al. [9], Tao et al. [22], and Doan et al. [23].

Global modelling approaches for PFHEs can be found in the literature. In [24–27], the authors carried out design optimizations of plate-fin heat exchangers by means of various algorithms. In all these works, the PFHE cores featured offset-strip extended surfaces in both the internal and external channels. The $\varepsilon - \mathrm{NTU}$ method was adopted to study the thermal performance. In the finned channels, head losses were computed by means of the Darcy–Weisbach formula. The values of friction factor and overall heat transfer coefficient were obtained by means of the correlations proposed by Manglik and Bergles [5]. Hao et al. [28] optimised the geometry of a compact heat exchanger equipped with offset-strip fins by means of the tree traversal method. The authors evaluated overall heat transfer performance with the heat current method, which allows one to obtain an equivalent thermal resistance based on the Inlet Temperature Difference (ITD) [29–31]. This approach does away with the tedious iterative procedure that comes with the LMTD-based resistance, and, with respect to the $\varepsilon - \mathrm{NTU}$ method, it is better suited for the analysis of the intricate networks of heat exchangers. Also in this case, the authors employed the correlations found in [5], obtaining a good agreement with experimental data.

With respect to the current approach, the models presented in the above-referenced works certainly have similar advantages in terms of ease of implementation and use, but they also feature shortcomings that may affect their accuracy. As will be shown later, the use of correlations from the literature can lead to significant deviations in the estimation of the thermo-hydraulic performance for particular geometries and operating fluids. Furthermore, the head losses produced by both manifolds and the influence of entrance effects on the overall heat transfer rates are two relevant aspects that are mostly neglected in the previously cited works.

1.3. Modelling Approach

In light of the above considerations, in the present work an original multiscale approach is proposed, compounding detailed 3D analyses at fin scale with global models at system scale, with the aim of obtaining accurate estimates of heat transfer rates and head losses of plate-fin heat exchangers, with reduced model complexity and at a reasonable overall computational cost. The proposed approach is specifically targeted towards engineering needs and is readily reproducible for a wide range of heat exchanger applications.

Figure 1 shows a simple diagram depicting the steps of the adopted modelling strategy, which are briefly introduced and discussed in the following:

i. The analysis starts with the characterization of the finned surfaces. The periodicity of these surfaces along the streamwise and spanwise directions is exploited to reduce the analysis of the entire channels to the study of fundamental units, under fully developed flow conditions. A detailed 3D CFD model is constructed for each different fin type, and a parametric analysis is carried out for different working fluids and several flow regimes, with the aim of deriving more general correlations describing their heat transfer and friction characteristics in terms of an overall Nusselt number, Nu, and an equivalent Darcy friction factor, f, respectively.

ii. Additional dedicated CFD analyses are also carried out to take into account entrance effects for both the Nusselt number and the equivalent friction factor. As previously discussed, these effects are seldom taken into account in common heat exchanger analysis, but they appear instead to be relevant, especially for the external channels of cross-flow plate-fin heat exchangers. In the present approach, the contribution of the developing flow in the entry region is accounted for by means of generalized correlations for suitable correction factors to both Nu and f, which are again derived from CFD results.

iii. Another aspect which is often overlooked in the assessment of heat exchanger performance is the evaluation of the pressure drop in the inlet and outlet manifolds, which, as shown in the following, can account for more than 90% of the total head losses of the internal side. The proposed methodology encompasses the use of CFD, coupled with an equivalent porosity model, in order to calculate equivalent concentrated loss coefficients for the manifolds, and therefore provide a more accurate estimate of the head losses of the internal side.

iv. On the basis of the results of the previous steps, global models are developed to compute the heat rejection and mechanical energy losses of the complete heat exchanger. The global model for heat transfer is based on the classical $\varepsilon - \mathrm{NTU}$ method [1], where the overall heat transfer coefficients are obtained by combining the correlations for the Nusselt number in fully developed flow—step (i) above—with the correction factors for the entry region—step (ii)—where appropriate. Head losses are instead computed using the empirical relations for friction factor derived in step (i), the correction factors for the entry region in the internal channels—step (ii)—and the concentrated loss coefficients for the inlet and outlet manifolds—step (iii).

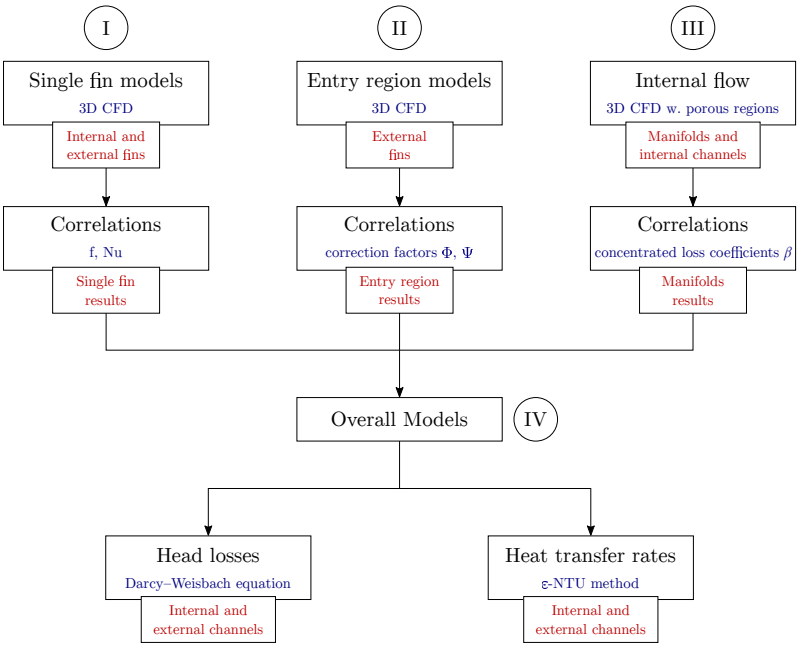


Figure 1. Simple schematic describing the modelling strategy adopted for the development of a high fidelity virtual model for PFHE heat exchangers.

In the following, the above-described detailed computational models and global models for heat transfer and head losses are introduced and described in detail, using a selected set of PFHE configurations as the case study. Friction factors and Nusselt numbers obtained from the numerical analyses are also compared with the data presented by Joshi and Webb [7], Manglik and Bergles [5], Awad and Muzychka [32], and Dong et al. [17], to assess whether or not the correlations already available in the literature are suitable for

predicting the performance of fins used in industrial applications. As will be shown in the following, the available correlations exhibit a fair agreement with most of the present results, but large uncertainties are present for several configurations of geometry and flow. Therefore, the present work, besides proposing a holistic approach being instrumental for a specific industrial use, provides additional insight on the research effort still needed to accurately characterize a wide category of fin geometries of great applicative interest.

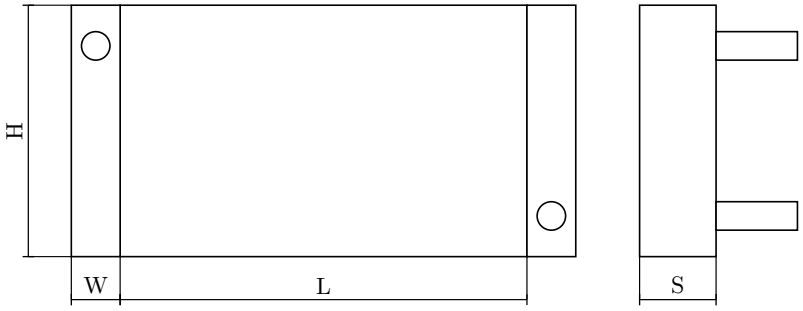
Finally, the proposed multiscale approach is validated by comparing global numerical results on head losses and heat transfer with available experimental data, for a considerable variety of heat exchanger configurations.

2. Materials and Methods

2.1. Case Study

In the present work, a set of eight plate-fin heat exchangers is considered, consisting of three air–oil coolers, two water–glycol radiators, and three charge air coolers. All these heat exchangers feature manifolds with a simple box shape and main pipes with a round cross-section and a diameter of 35 mm. The height, width, and depth of the manifolds are denoted by H, W, and S, respectively. The core of each heat exchanger is composed of N_{ch} internal channels and $N_{ch} + 1$ external ducts. The length of the core is identified by L. Figure 2a depicts a schematic showing the geometric features of the heat exchangers examined, along with some relevant dimensions, while Figure 2b depicts a picture of one of the actual heat exchangers considered. Table 1 reports the geometric characteristics of each heat exchanger, along with an identification code for future reference. The letter stands for the type of internal fluid, specifically O for oil, G for a water–glycol solution, and A for compressed air, while the number indicates the thickness of the heat exchanger in millimetres.

The heat exchangers under consideration feature finned surfaces with offset-strip and wavy geometries. The oil and water coolers have internal channels equipped with offset-strip fins and present external channels with wavy fins. On the other hand, the air-to-air heat exchangers are equipped with wavy fins in both the internal and external channels. The OSF employed in the oil coolers, designated as OSF1, presents a centred offset, and its front and top views are represent in the drawing of Figure 3a. The fin OSF2 is used in water–glycol radiators and, in comparison to the OSF1, features a larger aspect ratio and offset length. Moreover, in OSF2 the offset is not symmetric. The geometric differences between OSF1 and OSF2 can be clearly seen by comparing Figure 3a,b. Oil coolers and air-to-air heat exchangers present external finned surfaces with a wavy geometry with a triangular cross-section. This fin is identified by the acronym WF1, and its front and top views are depicted in the drawing of Figure 3c, along with the key dimensions. The WF2 fin features the same triangular cross-section and axial development as WF1, but it is has different values of pitch and height. The internal channels of the three charge air coolers present wavy fins with a rectangular cross-section, as illustrated in Figure 3d. This fin geometry is identified by the acronym WF3. WF4 is a wavy fin with a rectangular cross-section and sinusoidal development, as shown in Figure 3e. It is employed in the external channels of the two water–glycol radiators, designated as G94 and G113. The values of the geometric parameters of all the examined fins are presented in Table 2.



(**a**)



(**b**)

Figure 2. Sketch of the external geometry (**a**) and an example of a plate-fin heat exchanger, provided by VEMA S.r.l. (**b**).

Table 1. Identification codes, geometric parameters, and finned surfaces of the plate-fin heat exchangers examined.

ID	*S* [mm]	*H* [mm]	*W* [mm]	*L* [mm]	N_{ch}	Internal Fin	External Fin
O80	80	304	60	500	20	OSF1	WF1
O94	94	309	60	500	21	OSF1	WF1
O113	113	305	60	500	20	OSF1	WF1
G94	94	309	60	500	23	OSF2	WF4
G113	113	309	60	500	23	OSF2	WF4
A80	80	304	60	500	17	WF2	WF1
A94	94	304	60	500	17	WF3	WF1
A113	113	304	60	500	17	WF3	WF1

Table 2. Identification codes and geometric parameters of the finned surfaces examined.

ID	*x* [mm]	*y* [mm]	*l* [mm]	*a* [mm]	*t* [mm]
OSF1	1.5	3.0	5.0	-	0.2
OSF2	4.0	2.0	30.0	-	0.2
WF1	5.1	9.5	7.0	1.0	0.2
WF2	5.0	6.5	7.0	1.0	0.2
WF3	5.0	6.5	7.0	0.6	0.2
WF4	6.0	9.5	6.35	0.85	0.2

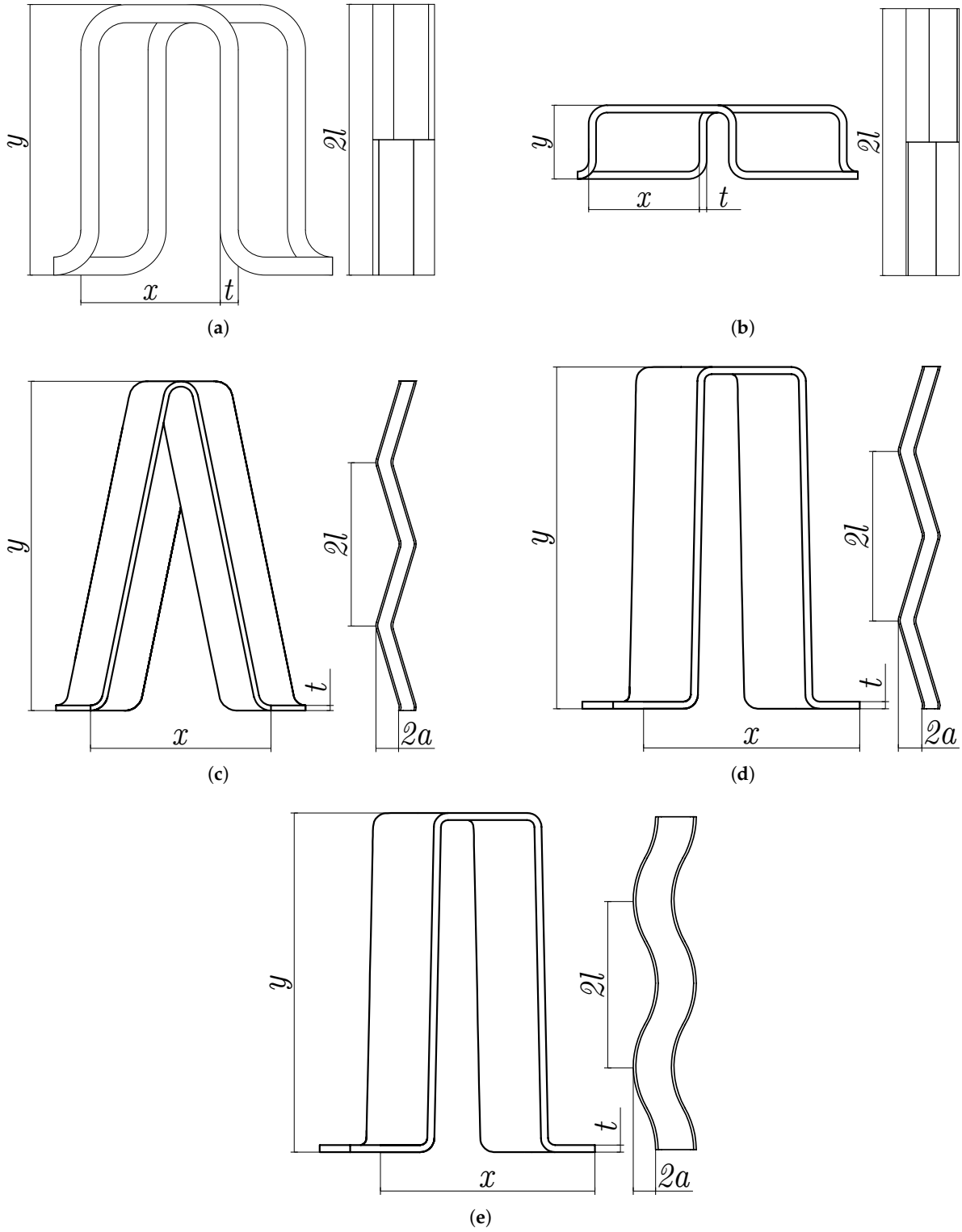


Figure 3. Front and top views of the fins: OSF1 (**a**), OSF2 (**b**), WF1 (**c**), WF2 (**c**), WF3 (**d**), and WF4 (**e**).

2.2. Single-Fin Model

Single fins are modelled in terms of their smallest unit geometry, which is repeated along the width and length of the channels. These basic modules are assumed to be located away from the inlet and outlet sections, so that the flow can be considered as fully developed. The flow is also assumed steady and incompressible for all the fluids and fins studied.

2.2.1. Governing Equations

In fluid regions, flow and temperature fields are determined by numerically solving momentum, continuity, and energy equations.

$$\begin{cases} \nabla \cdot (\rho \, \vec{v} \otimes \vec{v}) = -\nabla p + \nabla \cdot [\rho \, (\nu + \nu_t) \, \nabla \vec{v}] \\ \nabla \cdot \vec{v} = 0 \\ \nabla \cdot (\rho \, c_{\mathrm{p}} \, \vec{v} \, T) = \nabla \cdot (\lambda \nabla T) \end{cases} \tag{1}$$

Within the walls of the fins, temperature is obtained from the numerical solution of the heat conduction equation.

$$\nabla \cdot (\lambda_{\mathrm{s}} \nabla T) = 0 \tag{2}$$

Low Reynolds number flows are solved by performing laminar analyses, meaning that $\nu_t = 0$. This approach is maintained for increasing Re as long as a solution with a satisfactory degree of numerical convergence is reached; that is, when all residuals are of the order of 10^{-6}. The *k*-ω SST turbulence model is used for Reynolds number values that do not allow for a steady-state laminar solution. This turbulence model is selected among all the others as it is the one that leads to the best agreement between numerical and experimental results for offset-strip fins, according to Kim et al. [12].

To reduce the number of dimensional and flow parameters, the problem is reformulated in dimensionless form by scaling down the computational model by the reference length, chosen as the fin height, y. The problem is then defined by the Reynolds and Prandtl numbers alone. The fluid average velocity along the streamwise direction is assumed unitary, and the thermo-physical properties in Equation (1) are scaled accordingly:

$$\mu^* = \nu^* = \frac{1}{\mathrm{Re_y}} , \qquad c_{\mathrm{p}}^* = \mathrm{Re_y} \, \mathrm{Pr} \, . \tag{3}$$

Fins are made of 3003 aluminium alloy. The thermal conductivity of the solid walls is assumed constant with temperature and, in the adopted dimensionless framework, is obtained by scaling the thermal conductivity of aluminium by the one of the adjacent fluid.

$$\lambda_{\mathrm{s}}^* = \frac{\lambda_{\mathrm{alu}}}{\lambda_{\mathrm{fluid}}} \tag{4}$$

2.2.2. Boundary Conditions

To account for the periodicity of geometry and flow along the streamwise direction, field values at the inlet and outlet boundaries of the domain are linked by suitable mappings: At the inlet section, the velocity and temperature distributions are mapped from the outlet patch, keeping their integral average values fixed. At the inlet patch, a zero-gradient boundary condition is assigned to the pressure field. At the outlet patch, zero-gradient boundary conditions are applied to the velocity and temperature fields, while a uniform reference value is assigned to pressure. Periodic conditions are enforced along the spanwise direction. At the top and bottom boundaries, the temperature gradient is set to an arbitrary non-zero value, to impose an entering heat flux. At the walls, no-slip conditions are applied to the velocity field and a zero pressure gradient is imposed. Finally, continuity of temperature and heat flux is enforced at all fluid–solid interfaces. The boundary conditions described herein are summarised in Table 3.

Table 3. Boundary conditions applied to the inlet, outlet, left and right boundaries, and top and bottom surfaces in fluid and solid regions of the single-fin model [33].

Region	Field	Inlet	Outlet	Left/Right	Top/Bottom	Fluid–Solid Interface
fluid	$\vec{v}$	mapped	zero-gradient	periodic	no-slip	no-slip
	p	zero-gradient	uniform value	periodic	zero-gradient	zero-gradient
	T	mapped	zero-gradient	periodic	fixed gradient	heat flux continuity
solid	T	zero-gradient	zero-gradient	periodic	fixed gradient	heat flux continuity

2.2.3. Spatial Discretisation

Numerical simulations are conducted using a conjugate heat transfer solver based on the Finite Volume numerical approach and implemented in the open source computational software OpenFOAM 7 [34]. Convective terms are discretised using upwind schemes of second-order accuracy, while diffusive terms are addressed with central schemes presenting explicit non-orthogonality corrections. A variant of the SIMPLE algorithm [35] is employed to decouple the pressure and velocity fields. Depending on the geometry, the dimensionless single-fin modules are discretized with block-structured and hybrid computational grids, using the commercial tool Pointwise. In hybrid meshes, boundary layers are obtained by means of an advancing front algorithm, starting from a 2D mesh produced by using Delaunay triangulation. In both hybrid and structured grids, fluid and solid regions are extruded as separate blocks to allow for the convenient set up of multi-region simulations using OpenFOAM's built-in tools. Figure 4 shows the top and front faces of the computational grids for two fin configurations, OSF1 and WF1.

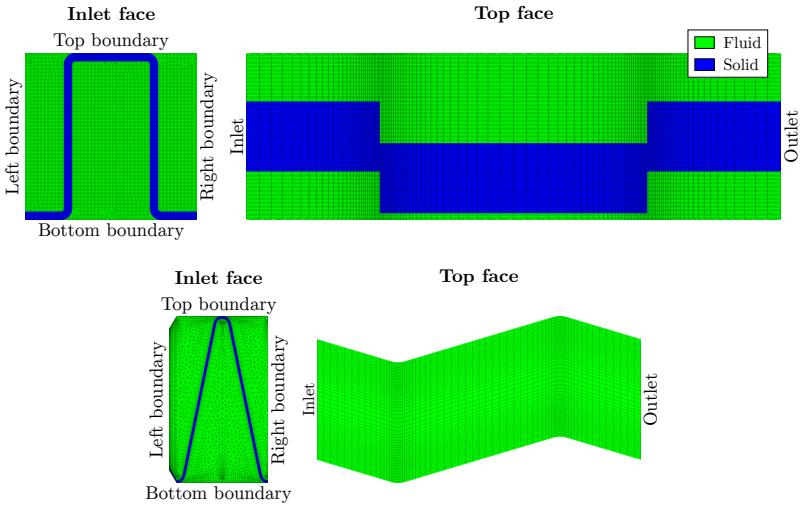


Figure 4. Selected cross-sections of the two computational meshes: OSF1 (**top**) and WF1 (**bottom**).

2.2.4. Mesh Sensitivity Analysis

Grid independence of single-fin models is investigated by comparing the values of friction factor obtained from three computational meshes of the WF1 fin, which are developed by halving the number of the base mesh elements each time, maintaining the same topology. Table 4 lists the f-values derived from the three computational grids at $\mathrm{Re_y} = 10,000$, along with the average cell size in the far field Δ^*, the near-wall element size Δ^*_w, and the number of elements of each computational grid. The obtained results are very close, as the difference between the medium and the coarse values is 0.9%, while the one between fine and medium values is 0.01%. The fine mesh is selected for all the following CFD analyses as it requires a lower number of iterations for the solution to converge, with

respect to the other grids. An analogous procedure was adopted for all of the fin geometries considered, leading to similar results.

Table 4. Friction factor values obtained from the coarse, medium, and fine meshes of WF1.

Grid	Δ^*	$\Delta_w{}^*$	Number of Cells	f	Difference to Previous Grid
Coarse	0.025	0.008	90×10^3	0.3982	-
Medium	0.020	0.004	180×10^3	0.4018	0.9%
Fine	0.016	0.002	360×10^3	0.4017	−0.01%

2.3. Numerical Model for Entrance Effects

The fully developed flow hypothesis can be considered valid for internal channels, for which entrance effects are negligible given the great ratio between the length of the channels and that of an elementary module. The external channels are much shorter; therefore, this hypothesis cannot be assumed valid a priori. The effects of flow development in the entry region on the thermo-hydraulic performance of the external finned surfaces are determined by means of dedicated CFD models comprising thirty single-fin modules in series, with the main aim of deriving the values of the Darcy friction factor and the Nusselt number of each module. The model also includes inlet and outlet tanks, and the analysis is performed on both of the external fins considered, WF1 and WF4. Similarly to the fully developed flow analyses, the flow is assumed steady and incompressible. Furthermore, the temperature and flow fields are obtained from the numerical solution of Equation (1), and by addressing the problem by the dimensionless framework described in Section 2.2. The governing equations are solved using the same algorithm and spatial discretisation schemes as those employed for single-fin models. In this case, as the analyses are performed considering air flows at medium to high Re-values, the k-ω SST turbulence model [36] is used for all the tested flow rates.

The main difference between the numerical models developed for fully developed flow and entrance region analyses, aside from the computational meshes, consists of the boundary conditions applied along the streamwise direction.

2.3.1. Boundary Conditions

At the inlet section, fluid velocity is set to a uniform value, to impose a unitary mean mean streamwise velocity within the fin stack. The value of fluid velocity at the inlet is derived by applying the mass conservation equation between the inlet section and the flow cross-section of the examined fin geometry. A uniform temperature value is set at the inlet, while a zero gradient boundary condition is assigned to pressure. At the outlet, pressure is constrained by setting a reference value for its integral mean, while a zero gradient boundary condition is applied to the velocity and temperature fields. Periodic conditions are enforced between the surfaces of the inlet and outlet domains. Table 5 summarises the boundary conditions considered for the entry region model.

Table 5. Boundary conditions applied to the inlet, outlet, left and right boundaries, and top and bottom surfaces in fluid and solid regions of the entry region model.

Region	Field	Inlet	Outlet	Left/Right	Top/Bottom	Fluid–Solid Interface
fluid	$\vec{v}$	uniform value	zero-gradient	periodic	no-slip	no-slip
	p	zero-gradient	fixed mean	periodic	zero-gradient	zero-gradient
	T	uniform value	zero-gradient	periodic	uniform gradient	heat flux continuity
solid	T	zero-gradient	zero-gradient	periodic	uniform gradient	heat flux continuity

2.3.2. Spatial Discretisation

The computational domains are discretised by means of hybrid meshes. The fin stacks are formed by replicating the respective grid developed for the fully developed flow study. The techniques involved in the generation of the grids for fully developed flow are mentioned in Section 2.2.3. The lengths of the entrance and egress domains are equal to ten and twenty times the height of the fin, respectively. The computational grids feature a block-structured topology close to the inlet and outlet surfaces, whereas unstructured sections are present in the vicinity of the fin stack. Figure 5 shows the computational grid developed to evaluate the effects of entrance flows in the WF1 finned surface.

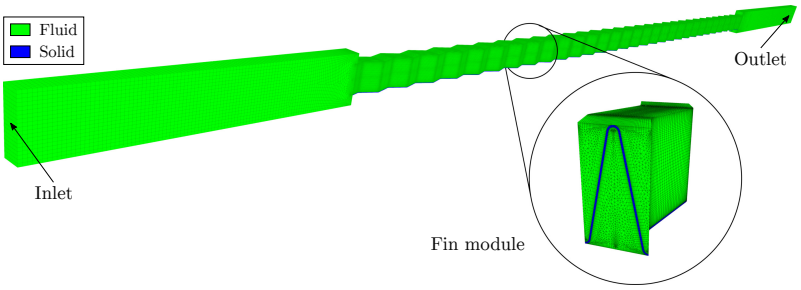


Figure 5. Entry region: computational mesh developed to study the entrance effect for the WF1 fin.

As stated previously, the computational grids for the entry region CFD models are developed on the basis of the meshes used for the fully developed flow analyses. Therefore, for the sensitivity analysis, the reader can refer to Section 2.2.

2.4. Head Losses in Inlet and Outlet Manifolds

2.4.1. Governing Equations

The head losses associated with the inlet and outlet manifolds are determined by developing a CFD model comprising the actual geometries of both manifolds, along with porous regions modelling the internal finned channels. Fluid flow is supposed steady, isothermal, and incompressible. The velocity and pressure fields are derived by numerically solving the steady-state RANS equations using the *k*-ω SST turbulence model [36].

$$\begin{cases} \nabla \cdot (\rho \, \vec{v} \otimes \vec{v}) = -\nabla p + \nabla \cdot [\rho \, (\nu + \nu_t) \, \nabla \vec{v}] - \rho \, \sigma_{\mathrm{m}} \\ \nabla \cdot \vec{v} = 0 \end{cases} \tag{5}$$

where σ_{m} is a momentum sink term that is non-zero only in porous regions, and it is defined on the basis of the Darcy–Forchheimer equation [37]:

$$\sigma_{\mathrm{m}} = \left(\nu \, \vec{D} + \frac{1}{2} \, \mathrm{tr}(\vec{v} \cdot I) \, \vec{F} \right) \vec{v} \, , \tag{6}$$

where the vectors $\vec{D}$ and $\vec{F}$ determine the loss of momentum given by the porous regions. These vectors are obtained by calibrating the equivalent porosity model. The Darcy–Weisbach equation is used to determine the pressure gradient given by a single internal channel for different velocity values:

$$\frac{\nabla p_{\mathrm{ch}}}{\rho} = \frac{f_{\mathrm{fd}} \, L}{2 \, y \, L_{\mathrm{m}}} \left(\frac{A_{\mathrm{ch,m}}}{A_{\mathrm{ch,r}}} \, v \right)^2 , \tag{7}$$

where f_{fd} is the Darcy friction factor, related to fully developed flow conditions, of the specific fin considered. f_{fd} is an outcome of the fully developed flow analyses, whose results are presented in Section 3.1. L_{m} is the length of the porous regions in the computational model.

The porous regions within the CFD model feature larger flow cross-sections than those of the real heat exchanger channels, due to the absence of fin walls. For this reason, fluid velocity is corrected by the term $A_{\mathrm{ch,m}}/A_{\mathrm{ch,r}}$, which is derived from the conservation equation in order to correctly evaluate the head losses in the internal channels. Finally, the streamwise components of $\vec{D}$ and $\vec{F}$ are determined by using a variant of the Levenberg–Marquardt algorithm [38] to fit Equation (6) to the $\nabla p_{\mathrm{ch}}/\rho$ and corrected velocity values. Figure 6 shows an example of this procedure applied to the G94 heat exchanger. The difference between the corrected and unchanged channel losses can be clearly seen, underscoring the importance of the term $A_{\mathrm{ch,m}}/A_{\mathrm{ch,r}}$, especially for large velocity values. In addition, the selected optimisation algorithm allows for a near perfect match between the momentum sink term S_{m} and the corrected $\nabla p_{\mathrm{ch}}/\rho$ values stemming from Equation (7). For this particular heat exchanger configuration, the values of $\vec{D}$ and $\vec{F}$ along the streamwise direction amount to $D_z = 67.85 \times 10^6$ m^{-2} and $F_z = 105.2$ m^{-1}. These are referred to as porous regions with a length of $L_{\mathrm{m}} = 40$ mm. The components of $\vec{D}$ and $\vec{F}$ along the x and y directions are set to one thousand times the value of the streamwise component, to enforce one-dimensional flow inside porous regions.

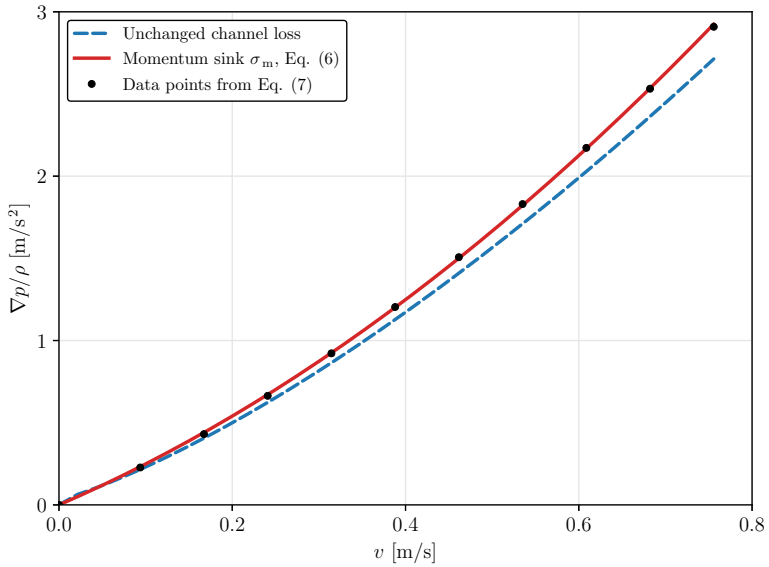


Figure 6. Comparison between the unchanged channel losses, the channel losses given by the calibrated porosity model, i.e., Equation (6), and the data points stemming from (7), which are employed for the curve fitting procedure.

2.4.2. Boundary Conditions

At the inlet section, a uniform velocity value is imposed, and a zero gradient boundary condition is assigned to pressure. At the outlet, the surface mean pressure is set to a reference value, and a zero gradient boundary condition is applied to the velocity field. At solid walls, no-slip conditions are employed. These boundary conditions are summarised in Table 6.

Table 6. Boundary conditions applied to the inlet, outlet, and walls of the computational model of the internal flow of the heat exchangers.

Field	Inlet	Outlet	Walls
$\vec{v}$	uniform value	zero-gradient	no-slip
p	zero-gradient	fixed mean	zero-gradient

2.4.3. Spatial Discretisation

The governing equations are solved numerically by means of an incompressible steady-state flow solver, which is based on the Finite Volume method and is implemented in OpenFOAM 7 [34]. The gradients are discretised through a linear Gauss scheme of second-order accuracy, whereas a first-order accurate upwind approach is employed for divergences. The convective terms and the pressure–velocity coupling are treated in the same way as in both the two types of models developed for the extended surfaces.

The computational domains are discretised with hybrid meshes using the same approach for all the configurations considered. The portions of the grid modelling the internal channels and the sections of the tanks away from inlet and outlet pipes are obtained using simple bottom-up block structured algorithms available in Pointwise. The sections of the manifolds close to the pipes are modelled using unstructured blocks extruded from 2D hybrid grids, where inflation layers are built using the same techniques described in Section 2.2.3. The simplified geometry resulting from the use of equivalent porous regions for the representation of internal channels allows for a substantial reduction of the number of elements included in the grid. The length of the inlet and outlet pipes is set to twenty times their diameter, to allow for correct flow development. The pipes are discretized with a butterfly-style grid, which is smoothed by means of a variant of the Thomas–Middlecoff algorithm [39] implemented in Pointwise. Figure 7 shows the selected views of the computational grid developed for the O94 heat exchanger.

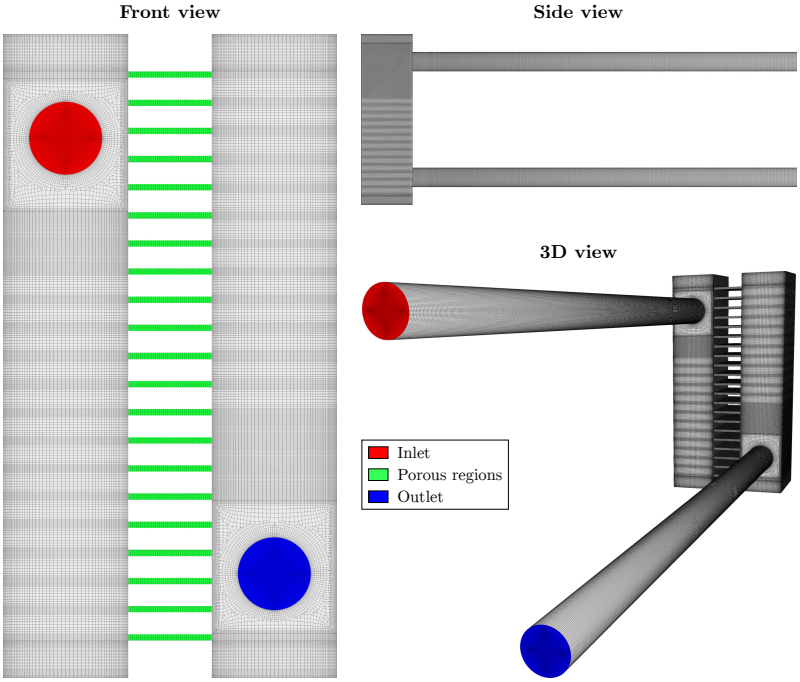


Figure 7. Sample mesh of the overall model for internal head losses, related to the O94 oil cooler.

2.4.4. Mesh Sensitivity Analysis

To evaluate the dependence of numerical results on the resolution of the mesh, three computational grids with the same topology are developed, with sizes of 6, 13, and 26 million elements, respectively. Table 7 shows the values of pressure difference obtained from the coarse, medium, and fine meshes of the A94 charge air cooler at $\mathrm{Re}_{\mathrm{D_p}} = 285 \cdot 10^3$, along with the number of elements of each grid, and the average size of cells in the far field, Δ, and near the walls, Δ_{w}. The Δp-values are evaluated between cross-sections located in the same positions as the pressure taps used during the experimental tests. The medium mesh is selected for all the following CFD analyses, as the deviation of 1.43% between

the results obtained from the medium and fine meshes is deemed acceptable, particularly when considering the substantial savings in computational effort that can be achieved by using the medium grid. An analogous procedure is adopted for all the heat exchanger models, yielding similar results.

Table 7. Pressure drop values obtained from the coarse, medium, and fine meshes of A94.

Grid	Δ [mm]	Δ_w [mm]	Number of Cells	Δp [kPa]	Difference to Previous Grid
Coarse	1.62	0.4	6×10^6	22.47	-
Medium	1.25	0.2	13×10^6	23.46	2.94%
Fine	0.99	0.1	26×10^6	23.13	1.43%

2.5. Global Models

2.5.1. Heat Transfer

The global thermal model for plate-fin heat exchangers is based on the $\varepsilon - \mathrm{NTU}$ method. The product between the equivalent heat transfer coefficient and the heat transfer surface is obtained by considering the series of thermal resistances related to the internal and external flows.

$$UA = \frac{1}{R_{\mathrm{int}} + R_{\mathrm{ext}}} = \frac{1}{\frac{1}{U_{\mathrm{int}} A_{\mathrm{int}}} + \frac{1}{U_{\mathrm{ext}} A_{\mathrm{ext}}}} \tag{8}$$

The internal global heat transfer coefficient, U_{int}, is determined by employing the Nusselt number correlation, for fully developed flow, of the specific fin considered. This correlation is a result stemming from the single-fin model. It is presented in Equation (20), as part of Section 3.1. The heat transfer coefficient associated with the external channels is obtained from the respective value of the Nusselt number, which is derived from the product of two contributions: (i) the fully developed Nu value, derived from Equation (20); (ii) the average Nusselt variation with respect to its fully developed value in the entrance region:

$$\overline{\mathrm{Nu}}_{\mathrm{e}} = \frac{1}{\frac{S}{2l} - 1} \int_1^{\frac{S}{2l}} \Psi(\chi)\, d\chi\,, \tag{9}$$

where $\Psi(\chi)$ expresses the Nusselt number variation with respect to the position of each elementary module within the external channels, and the Reynolds number. This is a result of the entry region study and is presented in Section 3.2. Internal and external heat transfer areas A_{int} and A_{ext} are obtained by multiplying the heat transfer area of the single-fin module by the number of modules. The effectiveness of the heat exchanger is computed considering both internal and external fluids unmixed in a cross-flow configuration.

$$\varepsilon = 1 - \exp\left[\frac{C_{\max}}{C_{\min}} \mathrm{NTU}^{0.22} \left\{\exp\left[-\frac{C_{\min}}{C_{\max}} \mathrm{NTU}^{0.78}\right] - 1\right\}\right] \tag{10}$$

Finally, the heat transferred between the two fluids is given by:

$$\dot{Q} = \varepsilon\, C_{\min}\, (T_{\mathrm{int,i}} - T_{\mathrm{ext,i}})\,. \tag{11}$$

The thermo-physical properties of the internal and external fluids are computed as a function of the mean temperature between the respective inlet and outlet sections. The computation of $\dot{Q}$ is performed iteratively by updating the values of fluid properties at each step of the procedure, until convergence is reached.

2.5.2. Internal Head Losses

Internal head losses are computed by summing the losses in the inlet and outlet manifolds and in the internal channels:

$$\Delta p_{\,\mathrm{int}} = \frac{1}{2}\,\rho_{\,\mathrm{i}}\,\beta_{\,\mathrm{i}}\,v_{\,\mathrm{i}}^{2} + \Delta p_{\,\mathrm{ch}} + \frac{1}{2}\,\rho_{\,\mathrm{o}}\,\beta_{\,\mathrm{o}}\,v_{\,\mathrm{o}}^{2}\,, \tag{12}$$

where $\beta_{\,\mathrm{i}}$ and $\beta_{\,\mathrm{o}}$ are the concentrated loss coefficients of the inlet and outlet manifolds, respectively. These values are derived from the CFD model presented in Section 2.4. The values of channel losses, $\Delta p_{\,\mathrm{ch}}$, in oil coolers and water radiators are derived from the Darcy–Weisbach equation:

$$\Delta p_{\,\mathrm{ch}} = \frac{1}{2}\,\rho\,f_{\,\mathrm{fd}}\,\frac{L}{y}\,v_{\,\mathrm{ch}}^{2}\,. \tag{13}$$

In charge air coolers, large temperature differences are often observed between the inlet and outlet of the internal channels. This causes significant variations in the thermophysical properties of the air, and hence in the local Reynolds number. Therefore, the head losses in the internal channels of charge air coolers are computed using a self-built numerical code to fully account for fluid temperature variations. The air mass flow rate is assumed to be uniformly distributed among internal channels. Air density is determined by means of an incompressible ideal gas law, considering a molar mass of 28.97 g/mol. Specific heat and dynamic viscosity are derived from the linear interpolation of tabled data. The temperature field in the channels is determined by solving the thermal energy global balance.

$$\int_{A} \rho\,c_{\,\mathrm{p}}\,T\,\vec{v}\cdot\vec{n}\,dA \;=\; U_{\,\mathrm{ch}}\int_{A}\left(\,T_{\infty}-T\,\right)dA \tag{14}$$

where $U_{\,\mathrm{ch}}$ is the global heat transfer coefficient of a single channel which is obtained from Equation (8). At the channel inlet, the temperature is set to a uniform value, while at the outlet a zero gradient condition is enforced. Equation (14) is numerically solved by using a staggered Finite Volume method, uniformly discretising the domain of a single internal channel in a series of successive sub-channels. Equation (14) is applied at the intersections between two sub-channels by considering control volumes encompassing half the volume of the fluid of each channel. The integrals are solved by means of the midpoint rule of second-order accuracy. The mean temperatures of the sub-channels are computed by upwind differencing of the values computed at the intersections. Once the temperature field is obtained, the density, velocity, and pressure fields are easily determined by means of the ideal gas law, mass conservation, and Equation (13) applied to each sub-channel.

2.5.3. External Head Losses

External head losses are determined by means of the well-known Darcy–Weisbach formula.

$$\Delta p_{\,\mathrm{ext}} = \frac{1}{2}\,\rho\,f_{\,\mathrm{fd}}\,\bar{f}_{\,\mathrm{e}}\,\frac{S}{y}\,v^{\,2} \tag{15}$$

The equivalent friction factor of external channels is given by the product of two components: (i) $f_{\,\mathrm{fd}}$, that is related to fully developed flow regime; (ii) $\bar{f}_{\,\mathrm{e}}$, which expresses the mean change of the friction factor in the entry region relative to its respective value for fully developed flow. The first of the two aforementioned contributions is obtained from the single-fin friction factor correlation (19), which is a result of the fully developed flows studies and is introduced later in Section 3.1. $\bar{f}_{\,\mathrm{e}}$ is obtained from the integral average of $\Phi(\chi)$, which expresses the variation of f, with respect to its fully developed value, as a function of the position of each single-fin module within the external channels and

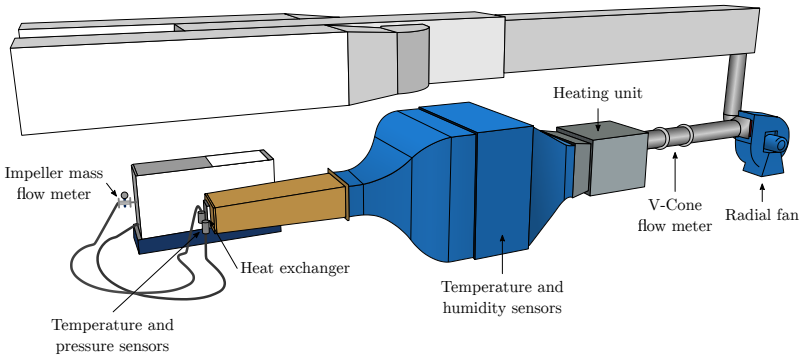
the Reynolds number. $\Phi(\chi)$ stems from the entry region study and is presented later in Section 3.2.

$$\bar{f}_e = \frac{1}{\frac{S}{2l} - 1} \int_1^{\frac{S}{2l}} \Phi(\chi)\, d\chi \tag{16}$$

Air properties are evaluated at the mean temperature between inlet and outlet sections; furthermore, the air outlet temperature is derived from the global heat transfer model, which is presented in Section 2.5.1.

2.6. Experimental Apparatus and Procedures

The experimental tests are conducted on the cooling component test bed of Virtual Vehicle Research GmbH, which is depicted in the schematic of Figure 8a. The test bed consists of a small open loop wind tunnel powered by a radial fan that can provide a maximum air mass flow rate of 3 kg/s. The heat exchangers are mounted at the end of the test section, which has the shape of a truncated pyramid, as shown in Figure 8b.



(**a**)



(**b**)

Figure 8. Drawing of the experimental apparatus, in which the main components are highlighted (**a**), and a picture showing one of the examined heat exchangers mounted to the end of the test section of the wind tunnel (**b**).

The air mass flow rate is measured with a V-Cone flow meter (±0.5% accuracy), and then the air is heated up to the specified inlet temperature. Air temperature is measured by employing calibrated type K thermocouples, which have an estimated error of 0.2 K. The inlet air temperature and humidity are measured just before the contraction, while the outlet temperature is measured by twelve thermocouples arranged in three rows of four sensors each.

The internal flow rate of the heat exchanger is measured with an impeller device, which is equipped with a magneto-inductive sensor. The sensor employed for air and

water flows features an accuracy of ± 1.0%, while the one used for oil flows is accurate up to ±0.15% of the flow rate.

The internal flow temperatures are measured near the inlet and outlet sections of the heat exchanger by using calibrated Pt100 sensors, which have an estimated error of 20 mK. The pressure drops related to the internal and external flows are measured by differential pressure transducers. The pressure taps used in the wind tunnel have an accuracy of ±1.0%, while the ones employed for the internal flow are 0.25% accurate for all fluids.

For each heat exchanger, the internal and external head losses and heat exchanged are measured for four values of internal flow rate and for four to five values of external flow rate. Then, the values of internal and external head losses are averaged over the external and internal fluid flow rates, respectively, to obtain an average head loss for each flow rate.

From this point on, the different flow rates associated with internal flow in the heat exchangers will be identified by their corresponding inlet Reynolds number, $\mathrm{Re}_{\mathrm{D_p}}$, which is calculated on the basis of the diameter of the inlet and outlet pipes.

3. Results and Discussion

3.1. Single-Fin Model

In the following, the results of the CFD analyses are presented in terms of dimensionless velocity and temperature fields. The fluid temperature field is expressed in dimensionless form in terms of the temperature difference $\vartheta = (\overline{T}_{\mathrm{w}} - T)/(\overline{T}_{\mathrm{w}} - \overline{T}_{\mathrm{b}})$, where $\overline{T}_{\mathrm{w}}$ and $\overline{T}_{\mathrm{b}}$ are the average wall and bulk temperatures, respectively. The velocity and temperature fields are displayed by means of longitudinal cross-sections located at the half height of the fins. Figure 9 shows the velocity and temperature fields for the OSF1 fin, related to an oil flow at $\mathrm{Re}_{\mathrm{y}} = 100$. The laminar boundary layer growth is apparent, and behind each wall small wakes are formed due to flow separation. The dimensionless temperature field in Figure 9b shows a marked asymmetric distribution, despite the symmetric velocity field observed in Figure 9a. This behaviour is caused by the presence of fillet radii between the vertical and horizontal walls of the fin, which determine the formation of asymmetric half-channels at each fin interruption. In addition, this phenomenon seems to be emphasised by high values of the Prandtl number [33].

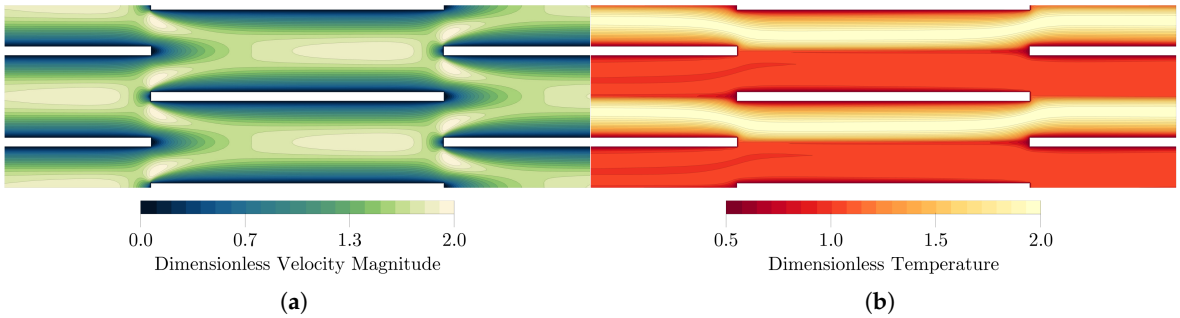
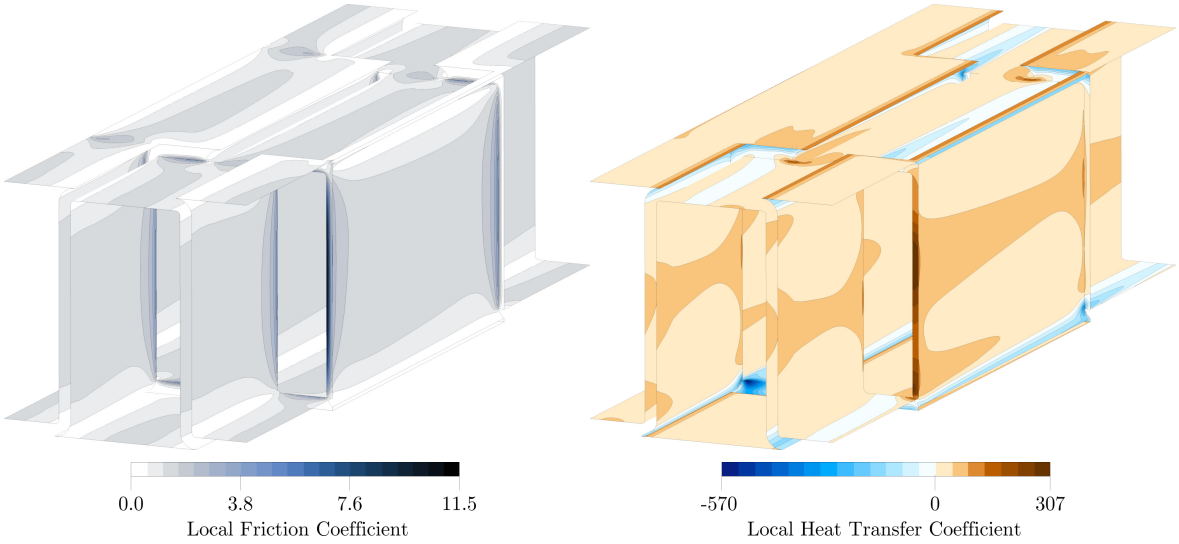


Figure 9. OSF1: Contour plots of dimensionless velocity magnitude (**a**) and temperature difference (**b**) along a longitudinal cross-section, as obtained by CFD at $\mathrm{Re}_{\mathrm{y}} = 100$ and Pr = 190. Dimensionless velocity colour scheme from [40].

Figure 10a shows the distribution of local friction coefficient on the walls of the fin: as expected, the maximum values are found near the leading edge of the walls and on the front faces. In this case the total friction resistance is worth about half of the total losses, meaning that the rest is given by pressure drag. The distribution of the local heat transfer coefficient (Figure 10b) of the OSF1 fin features maximum values near the leading edges and on the front faces of the walls, while the negative peaks are due to the hot current that heats the fin walls, as shown in Figure 9b.

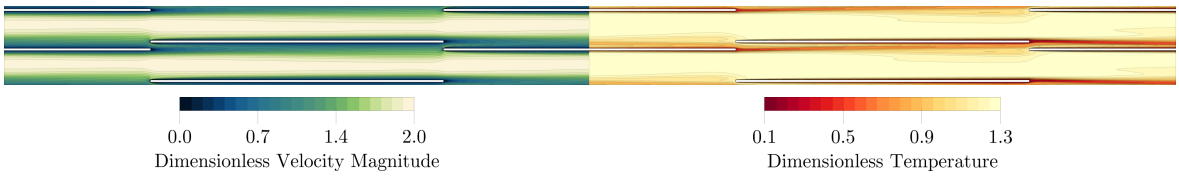
Figure 11 shows the dimensionless velocity and temperature fields of the OSF2 fin, corresponding to a flow of water at $\mathrm{Re_y} = 800$. In this case, the asymmetric offset determines a preferential path for the flow.

Figures 12 and 13 show the dimensionless velocity and temperature fields of the WF1 and WF4 fins, related to an air flow at $\mathrm{Re_y} = 10,000$, respectively. The two fins show similar velocity distributions: flow separations occur in correspondence to the troughs of the fins, while the maximum velocity values are found near the crests. As expected, temperature hot spots are present in correspondence to the flow recirculation regions. Similar results were obtained for WF2 and WF3. Figure 14a shows the local friction coefficient of the WF3 fin: skin friction drag is uniformly distributed on the walls, with slight maximum and minimum peaks are positioned in close proximity to the fin crests and troughs, respectively. The distribution of the local heat transfer coefficient shown in Figure 14b features regions of great heat transfer effectiveness at the half height of the fins, while regions of negative heat transfer coefficient are observed where the vertical walls of the fin form an angle of less than 90 degrees with the horizontal ones.



(**a**) (**b**)

Figure 10. OSF1: Distributions of local friction coefficient (**a**) and local heat transfer coefficient (**b**), as obtained by CFD at $\mathrm{Re_y} = 100$ and Pr = 190. Local friction coefficient colour scheme from [40].



(**a**) (**b**)

Figure 11. OSF2: Contour plots of dimensionless velocity magnitude (**a**) and temperature difference (**b**) along a longitudinal cross-section, as obtained by CFD at $\mathrm{Re_y} = 800$ and Pr = 7. Dimensionless velocity colour scheme from [40].

Integral results on head losses and heat transfer are presented in terms of the equivalent Darcy friction factor and the mean Nusselt number. The equivalent friction factor associated with single fins is obtained from the well-known Darcy–Weisbach formula, by substituting the hydraulic diameter with the height of fin:

$$f = \frac{y\,(\bar{p}_\mathrm{i} - \bar{p}_\mathrm{o})}{l\,\rho\,\bar{v}_\mathrm{i}^2}\,, \tag{17}$$

where overbars indicate integral mean field values over the inlet (i) and outlet (o) sections. The Nusselt number is evaluated from the average fluid bulk temperature between the inlet and outlet sections, $\overline{T}_{\mathrm{b}} = 0.5\,(T_{\mathrm{b,i}} + T_{\mathrm{b,o}})$:

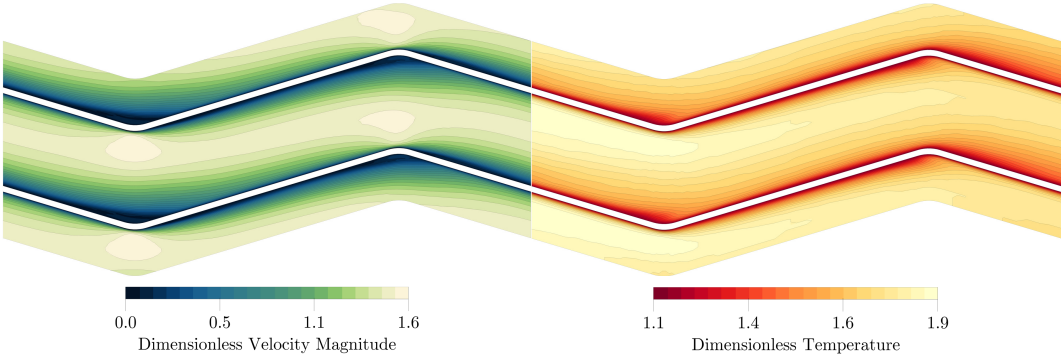
$$\mathrm{Nu} = \frac{\dot{Q}\,y}{\lambda\,A_{\mathrm{ref}}\,(\overline{T}_{\mathrm{w}} - \overline{T}_{\mathrm{b}})}\,, \tag{18}$$

where $\overline{T}_{\mathrm{w}}$ represents the integral mean temperature over the heat transfer surface A_{ref}, which includes the fluid–solid interfaces and the top and bottom patches. The values of Nusselt number and the friction factor derived from the CFD models are used to obtain correlations, as functions of the Reynolds number alone.

$$\log f_{\mathrm{fd}} = b_1\,\log^{b_2}\mathrm{Re}_{\mathrm{y}} + b_3 \tag{19}$$

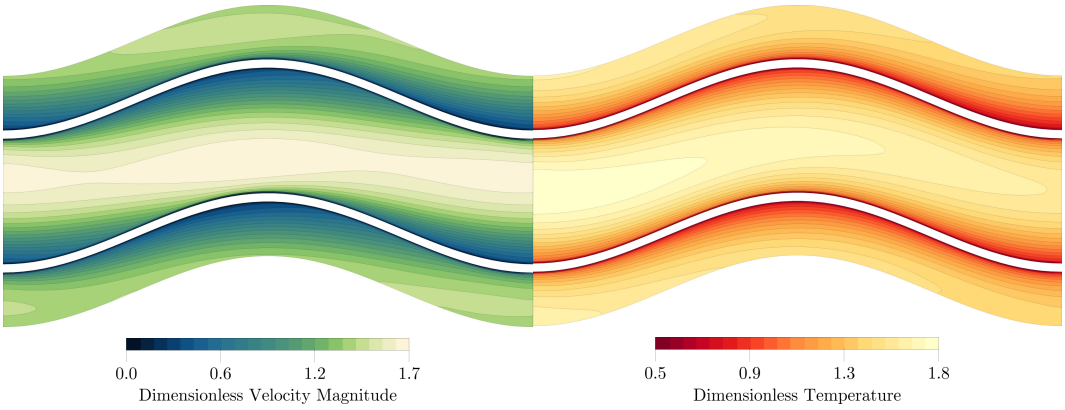
$$\mathrm{Nu}_{\mathrm{fd}} = c_1\,{\mathrm{Re}_{\mathrm{y}}}^{c_2} + c_3 \tag{20}$$

Since each fin is associated with a specific fluid depending on the type of cooler, the effect of Pr is included in the c_i coefficients. The values of the coefficients b_i and c_i are found by fitting Equations (19) and (20) to numerical results by means of a variant of the Levenberg–Marquardt algorithm [38], implemented in the SciPy library [41]. The values of b_i and c_i are reported in Table 8 for each fin.



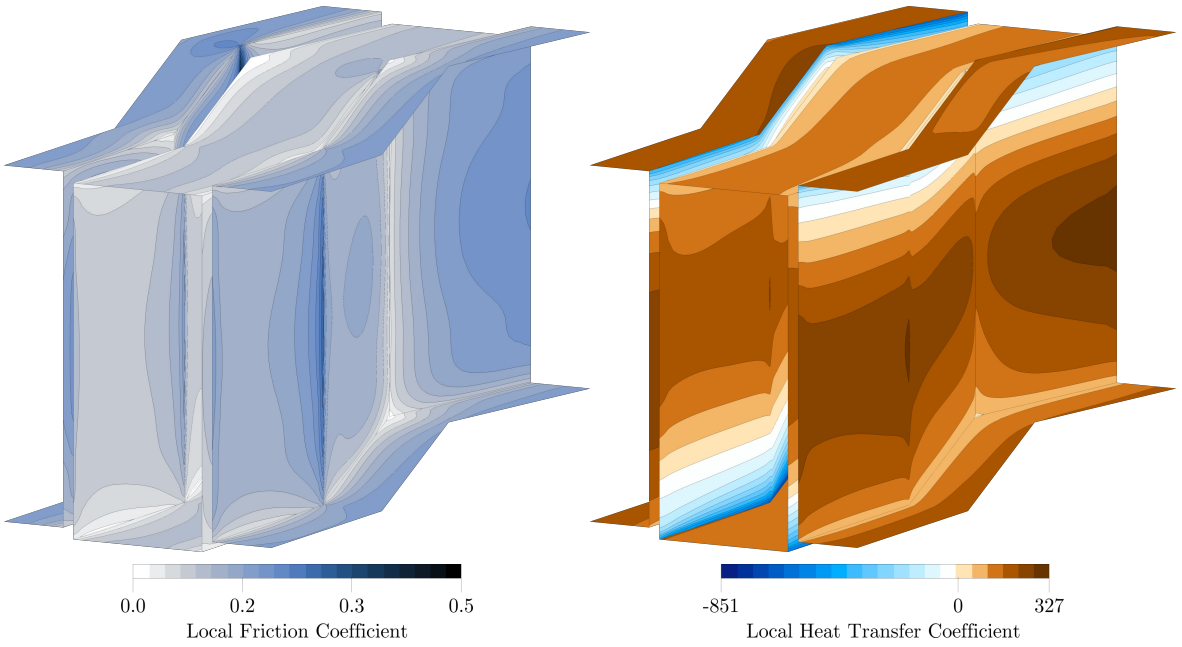
(**a**) (**b**)

Figure 12. WF1: Contour plots of dimensionless velocity magnitude (**a**) and temperature difference (**b**) along a longitudinal cross-section, as obtained by CFD at $\mathrm{Re}_{\mathrm{y}} = 10,000$ and Pr = 0.71. Dimensionless velocity colour scheme from [40].



(**a**) (**b**)

Figure 13. WF4: Contour plots of dimensionless velocity magnitude (**a**) and temperature difference (**b**) along a longitudinal cross-section, as obtained by CFD at $\mathrm{Re}_{\mathrm{y}} = 10,000$ and Pr = 0.71. Dimensionless velocity colour scheme from [40].



(**a**) (**b**)

Figure 14. WF3: Distributions of local friction coefficient (**a**) and local heat transfer coefficient (**b**), as obtained by CFD at $\mathrm{Re_y} = 10,000$ and Pr = 0.71. Local friction coefficient colour scheme from [40].

Table 8. Values of b_i and c_i coefficients in Equations (19) and (20).

ID	b_1	b_2	b_3	c_1	c_2	c_3	$\mathrm{Re_y}$-Range
OSF1	−1.704	0.646	3.043	0.020	1.392	10.22	$15 \leq \mathrm{Re_y} \leq 70$
				41.74	0.140	−57.89	$70 < \mathrm{Re_y} \leq 300$
OSF2	11.37	−0.247	−9.915	0.021	0.805	3.571	$100 \leq \mathrm{Re_y} \leq 2000$
WF1	−1418	0.0008	1419	0.028	0.862	10.51	$1000 \leq \mathrm{Re_y} \leq 30,000$
WF2	−1033	0.0012	1034	0.205	0.636	0.728	$800 \leq \mathrm{Re_y} \leq 10,000$
WF3	−5.635	0.158	6.490	0.045	0.832	2.621	$800 \leq \mathrm{Re_y} \leq 10,000$
WF4	2085	−0.0006	−2083	0.570	0.580	−16.46	$1000 \leq \mathrm{Re_y} \leq 30,000$

Numerical results of offset-strip fins are compared with those estimated by means of the correlations presented by Joshi and Webb [7]:

$$f_\mathrm{F} = 8.12\,\mathrm{Re}_{D_\mathrm{h}}^{-0.74}\left(\frac{l}{D_\mathrm{h}}\right)^{-0.41}\alpha^{-0.02}, \tag{21}$$

$$j = 0.53\,\mathrm{Re}_{D_\mathrm{h}}^{-0.5}\left(\frac{l}{D_\mathrm{h}}\right)^{-0.15}\alpha^{-0.14}, \tag{22}$$

and Manglik and Bergles [5]:

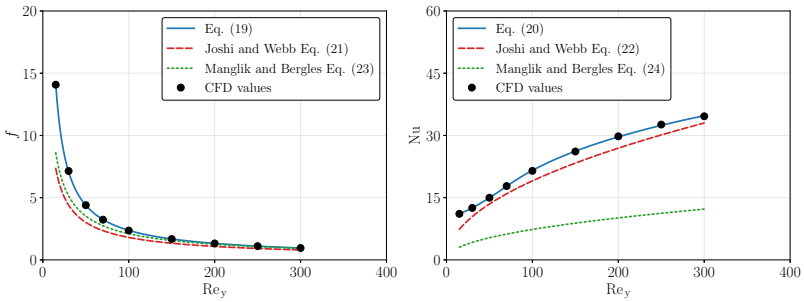
$$f_\mathrm{F} = 9.6243\,\mathrm{Re}_{D_\mathrm{h}}^{-0.7422}\alpha^{-0.1856}\delta^{0.3053}\gamma^{-0.2659}\left[1 + 7.669\cdot 10^{-8}\,\mathrm{Re}_{D_\mathrm{h}}^{4.429}\alpha^{0.920}\delta^{3.767}\gamma^{0.236}\right]^{0.1}, \tag{23}$$

$$j = 0.6522\,\mathrm{Re}_{D_\mathrm{h}}^{-0.5403}\alpha^{-0.1541}\delta^{0.1499}\gamma^{-0.0678}\times\left[1 + 5.269\cdot 10^{-5}\,\mathrm{Re}_{D_\mathrm{h}}^{1.340}\alpha^{0.504}\delta^{0.456}\gamma^{-1.055}\right]^{0.1}, \tag{24}$$

where α, δ, and γ are:

$$\alpha = \frac{x-t}{y-t}, \qquad \delta = \frac{t}{l}, \qquad \gamma = \frac{t}{x-t}. \tag{25}$$

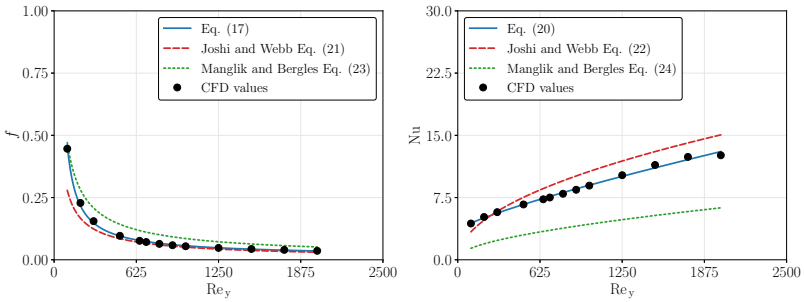
Figure 15 shows the comparison with the correlations available in the literature for the OSF1 fin, considering oil at Pr = 190 as the working fluid. There is a good agreement between the CFD f-values and those estimated by means of Joshi and Webb's correlation towards the upper end of the Re-range considered. The deviation grows with decreasing Reynolds, and at $Re_y = 15$ the numerical f-value is almost twice the one obtained from Equation (21). The model developed by Manglik and Bergles gives a better agreement, as the CFD values are exactly matched for $Re_y \geq 150$, and at low Re-values the deviations between numerical and estimated f-values are lower than those resulting from Joshi and Webb's model. Reynolds number values between 15 and 150 are typical of the internal channels of oil coolers. Therefore, an accurate prediction of the friction factor in this range is critical for a precise evaluation of the internal channel head losses. Both models developed by Joshi and Webb and Manglik and Bergles are seen to underestimate present numerical Nu-values. Both of these models were developed on the basis of experimental data on air and water flows. Therefore, significant deviations are expected when extrapolating them to a Pr-value of 190. In addition, the Chilton–Colburn analogy does not hold for laminar flows and values of Prandtl number greater than 160.



(**a**) (**b**)

Figure 15. OSF1: Friction factor (**a**) and Nusselt number (**b**) data: present study vs. literature (Pr = 190) [5,7].

The comparison between the numerical f-values obtained for OSF2 and the considered models from the literature leads to similar results to those observed for OSF1, as shown in Figure 16a. However, in this case, the most accurate estimation of numerical results is provided by Joshi and Webb's correlation. In this instance, the numerical Nu-values are overestimated by Joshi and Webb's model, while they are underestimated by Manglik and Bergles's correlation, as illustrated in the plot of Figure 16b. It should be noted that the correlations by Joshi and Webb and Manglik and Bergles were developed for offset-strip fins with a centred or symmetric offset, whereas OSF2 has an off-centre offset; therefore, deviations in the estimations of both f and Nu are to be expected.



(**a**) (**b**)

Figure 16. OSF2: Friction factor (**a**) and Nusselt number (**b**) data: present study vs. literature (Pr = 7) [5,7].

The values of f and Nu obtained from the CFD analyses for the wavy fins are compared with the models developed by Awad and Muzychka [32]:

$$
\begin{aligned}
f_{\mathrm{F}} &= \left(f_{\mathrm{F},1}^{2} + f_{\mathrm{F},2}^{2}\right)^{0.5}, \\
f_{\mathrm{F},1} &= 24\,\mathrm{Re}_{D_{\mathrm{h}}}^{-1}\,\frac{L_{\mathrm{e}}}{2l}\left(1 - 1.3553\,\alpha + 1.9467\,\alpha^{2} - 1.7012\,\alpha^{3} + 0.9564\,\alpha^{4} - 0.2537\,\alpha^{5}\right), \\
f_{\mathrm{F},2} &= 3.44\,\mathrm{Re}_{D_{\mathrm{h}}}^{-0.5}\left(\frac{D_{\mathrm{h}}}{0.5\,L_{\mathrm{e}}}\right)^{0.5},
\end{aligned}
\tag{26}
$$

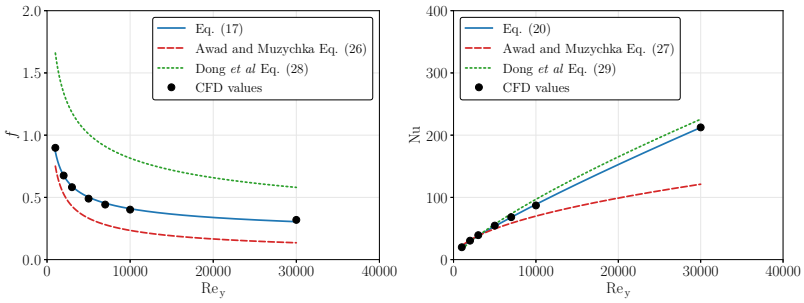
$$
\begin{aligned}
j &= \left(j_{1}^{5} + j_{2}^{5}\right)^{0.2}, \\
j_{1} &= \frac{7.541}{\mathrm{Re}_{D_{\mathrm{h}}}\,\mathrm{Pr}^{1/3}}\left(1 - 2.610\,\alpha + 4.970\,\alpha^{2} - 5.119\,\alpha^{3} + 2.702\,\alpha^{4} - 0.548\,\alpha^{5}\right), \\
j_{2} &= 0.664\,\mathrm{Re}_{D_{\mathrm{h}}}^{-0.5}\left(\frac{D_{\mathrm{h}}}{0.5\,L_{\mathrm{e}}}\right)^{0.5},
\end{aligned}
\tag{27}
$$

and Dong et al. [17]:

$$
f_{\mathrm{F}} = 1.16\,\mathrm{Re}_{D_{\mathrm{h}}}^{-0.309}\left(\frac{x}{2y}\right)^{0.3703}\left(\frac{x}{4a}\right)^{-0.25}\left(\frac{L_{\mathrm{d}}}{2l}\right)^{-0.1152}
\tag{28}
$$

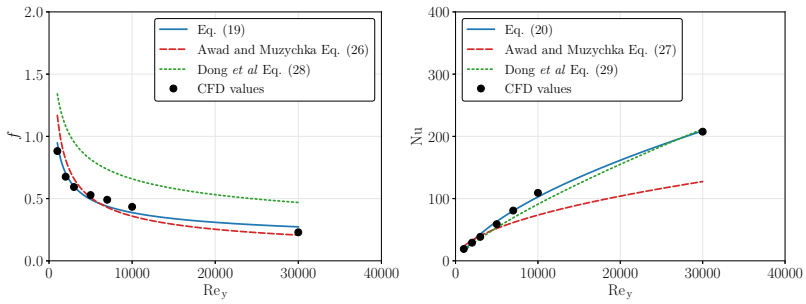
$$
j = 0.0836\,\mathrm{Re}_{D_{\mathrm{h}}}^{-0.2309}\left(\frac{x}{2y}\right)^{0.1284}\left(\frac{x}{4a}\right)^{-0.153}\left(\frac{L_{\mathrm{d}}}{2l}\right)^{-0.326}
\tag{29}
$$

Since the present work focuses on fully developed flow, the model presented by Dong et al. is slightly modified by discarding the terms related to the total wavy-fin length L_{d}. However, it should be noted that this modification leads to a loss of accuracy, since the model also loses its dependence on the wavelength. Figures 17 and 18 show values of friction factor and Nusselt obtained from CFD, the respective correlations derived from numerical results, and the comparison with data from the literature for WF1 and WF4. For both geometries, the modified correlation by Dong et al. overestimates the present numerical f-values, while the analytical model by Awad and Muzychka is in better agreement with the CFD values, particularly for WF4. The numerical Nu-values are matched by Awad and Muzychka's relations with small deviations at low Re values, while the mismatches increase with the Re and are maximum for $\mathrm{Re_y}$ =30,000. The values of Nusselt number estimated by means of the correlation by Dong et al. are in good agreement with CFD values, as the observed deviations are of ±20% at most. Similar results were found for WF2 and WF3.



(**a**) (**b**)

Figure 17. WF1: Friction factor (**a**) and Nusselt number (**b**) data: present study vs. literature [17,32].



(**a**) (**b**)

Figure 18. WF4: Friction factor (**a**) and Nusselt number (**b**) data: present study vs. literature [17,32].

Overall, the correlations proposed in the literature are adequate for the calculation of the friction factor for the geometries and flow regimes considered. In most cases, noticeable deviations were found regarding the prediction of the Nusselt number. The uncertainties related to the estimations done by means of the correlations by Dong et al. for both f and Nu may be attributed to the modifications done to adapt the model for fully developed flow. The analytical model by Awad and Muzychka performs much better for the estimation of f, while significant deviations are observed when estimating the values of the Nusselt number. It must also be emphasized that the multitude of possible combinations of the dimensional parameters of the fins makes it very difficult, if not impossible, to define universal correlations. The CFD analyses presented here not only provide accurate and reliable results for the specific geometries analysed in this work, but also constitute an additional set of results that may be useful to broaden the range of validity of possible general correlations.

3.2. Entry Region

The results of the CFD analyses on velocity and temperature fields are presented by means of contour plots of dimensionless streamwise velocity component and temperature $\vartheta = (\overline{T}_{\mathrm{w}} - T)/(\overline{T}_{\mathrm{w}} - \overline{T}_{\mathrm{b}})$, on spanwise-centred vertical cross-sections, which include the first fifteen single-fin modules.

Figure 19 shows the dimensionless velocity and temperature fields obtained for WF1. Near the inlet of the fin stack, flow separations are present along the lower and upper edges and along the leading edge of the walls of the fins. Figure 19b shows the dimensionless temperature field, which reaches full development roughly near the fifteenth module. Figure 20 shows the dimensionless streamwise velocity and temperature fields of WF4. As for WF1, the flow separates near the sharp edges in correspondence to the inlet section. Both the velocity and the temperature fields are fully developed by the fifteenth single fin module.

Entrance effects on head losses and the heat transfer effectiveness of WF1 and WF4 are evaluated by computing the deviation of the Darcy friction factor and Nusselt number with respect to the corresponding fully developed values, for each j-th single-fin module:

$$\Phi_j = \log\left(\frac{1}{f_{\mathrm{fd}}}\frac{y\,(\bar{p}_{\mathrm{i},j} - \bar{p}_{\mathrm{o},j})}{l\,\rho\,\bar{v}^2_{\mathrm{i},j}}\right), \tag{30}$$

$$\Psi_j = \frac{1}{\mathrm{Nu}_{\mathrm{fd}}}\frac{\dot{Q}_j\,y}{\lambda\,A_{\mathrm{ref}}\,(\overline{T}_{\mathrm{w},j} - \overline{T}_{\mathrm{b},j})}. \tag{31}$$

Figures 21a and 22a show that, for both fin geometries, there is a strong increase of the friction factor for the first unit module, equal to three times the fully developed value

for WF1 and four times for WF4. On the other hand, for the next four to six modules, f decreases with respect to f_{fd}, and the lowest valleys are found for the lowest among the Re-values considered. For both geometries, the friction factor becomes stable around the tenth single-fin module. In both cases, in correspondence to the thirtieth module, f grows slightly due to the sharp edge present at the outlet of the fin stack. The variation of the Reynolds number does not cause significant changes of entrance effects on the friction factor.

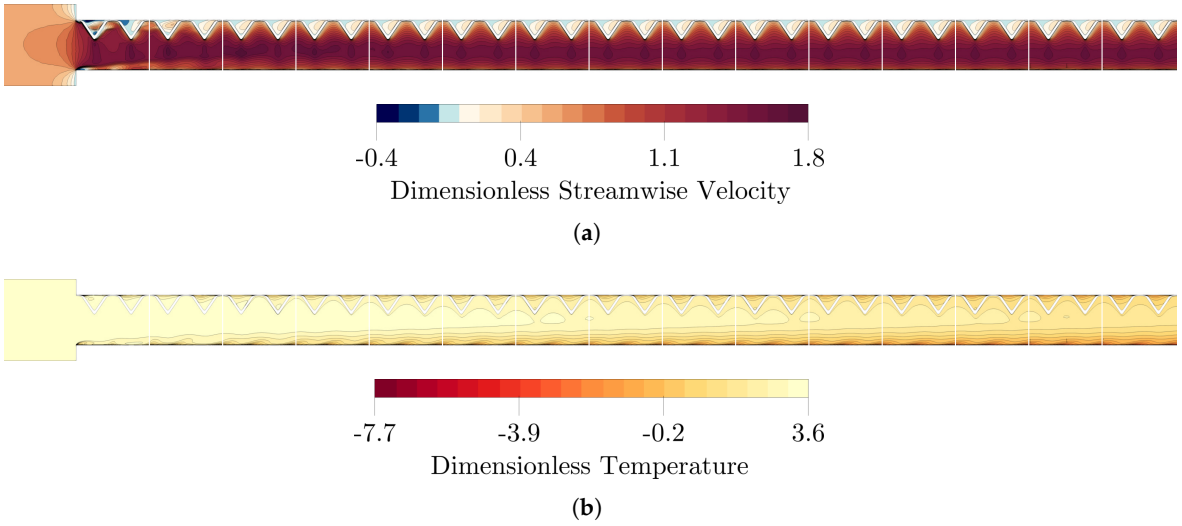


Figure 19. WF1 entrance region: Contour plots of dimensionless streamwise velocity component (**a**) and dimensionless temperature (**b**) of the first fifteen elementary modules, obtained by CFD at $Re_y = 10,000$ and $Pr = 0.71$.

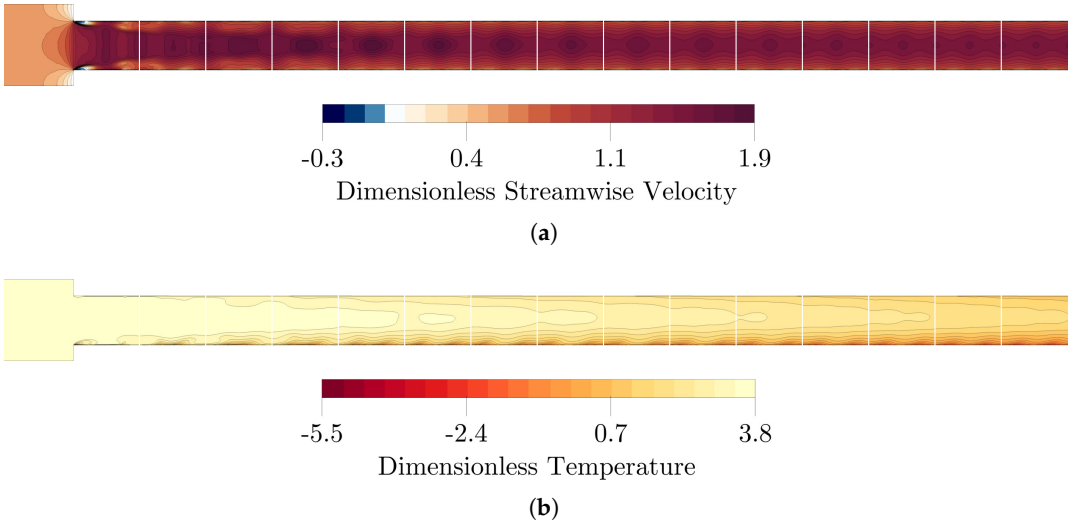
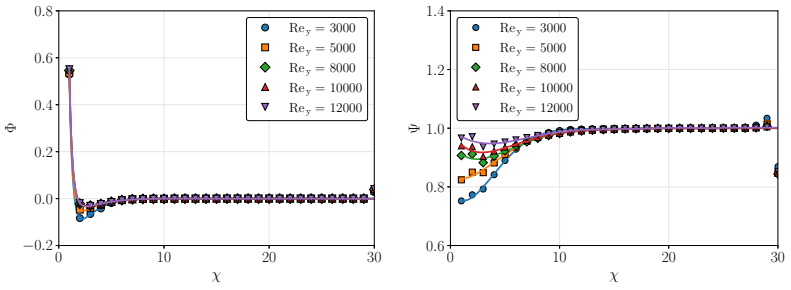


Figure 20. WF4 entrance region: Contour plots of dimensionless streamwise velocity component (**a**) and dimensionless temperature (**b**) of the first fifteen elementary modules, obtained by CFD at $Re_y = 10,000$ and $Pr = 0.71$.

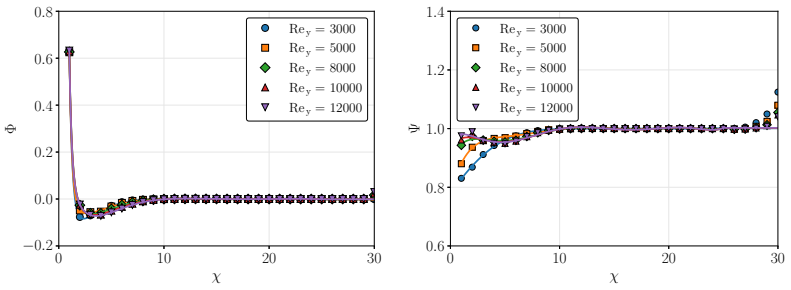
Figures 21b and 22b show the variation of Nusselt number in the entrance region for WF1 and WF4, respectively. In both cases, Nu increases with each fin module until it reaches its fully developed value near the tenth fin module. WF1 shows a greater sensitivity to the Reynolds number compared to WF4, and in both cases, as Re_y increases entrance effects become less relevant. The decreased heat transfer effectiveness observed in the entrance region is a result of the misalignment between the flow and the fin walls at the inlet of the channel, which leads to the formation of large separation bubbles that reduce local heat transfer effectiveness in the entrance region. In general, these distributions of Nusselt

number show opposite trends to those usually observed for straight-walled channels and fins, in which Nu is higher in the entrance region and decreases as the flow develops.



(**a**) (**b**)

Figure 21. WF1 entrance region: Values of relative friction factor (**a**) and Nusselt number (**b**) as a function of the position of each single-fin unit.



(**a**) (**b**)

Figure 22. WF4 entrance region: Values of relative friction factor (**a**) and Nusselt number (**b**) as a function of the position of each single-fin unit.

The results of the CFD analyses are employed to derive correlations that express the variations of f and Nu with respect to their fully developed values as a function of the module number χ and Reynolds number. The friction factor and Nusselt deviations due to outlet effects are not considered.

$$\Phi = \sum_{k=0}^{7} \sum_{r=0}^{4} d_{kr} \, \mathrm{Re_y}^{r} \log^{k} \chi \tag{32}$$

$$\Psi = \sum_{k=0}^{7} \sum_{r=0}^{4} e_{kr} \, \mathrm{Re_y}^{r} \chi^{k} \tag{33}$$

The values of the coefficients d_{kr} and e_{kr} have been omitted for the sake of brevity, while the correlations, along with the CFD results, are shown in Figures 21 and 22.

3.3. Head Losses in Inlet and Outlet Manifolds

Figure 23 displays contour plots of dimensionless velocity at $\mathrm{Re_{D_p}} = 2200$, related to the O94 heat exchanger. These colour maps are obtained on cross-sections located at the mid-planes of the inlet and outlet pipes, respectively. In the inlet tank, the fluid enters at high speed, impinging the wall opposite the entrance. The redistribution of the fluid across the wall generates two large-scale vortices. Fluid velocity is much more uniform in the outlet manifold, while near the outlet pipe it increases sharply, forming two recirculation regions, which cause major head losses, by restricting the effective outflow section.

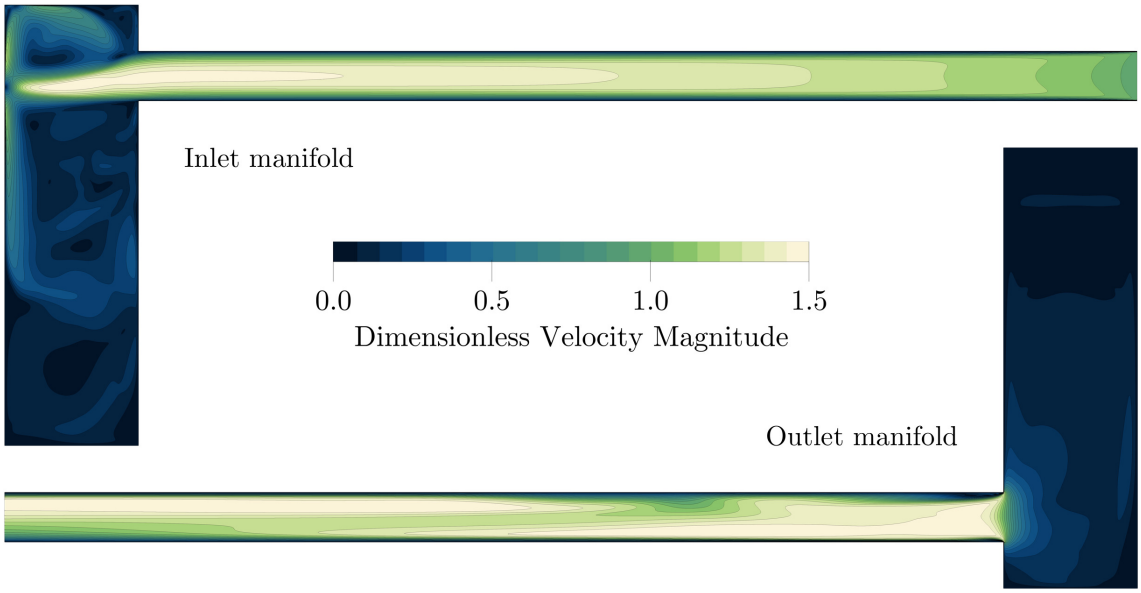


Figure 23. Global head losses model: Contour plots of dimensionless velocity magnitude of inlet and outlet manifolds of O94 on vertical cross-sections. Colour scheme from [40].

Head losses associated with inlet and outlet manifolds are computed by means of the numerical models presented in Section 2.4, considering the integral mean values of the pressure field evaluated on cross-sections corresponding to the connection between the channels and the manifolds, and the locations of the pressure taps positioned in the inlet and outlet pipes of the heat exchangers during the experimental tests. The resulting values of Δp_{i} and Δp_{o} are employed to compute the concentrated loss coefficients of the inlet and outlet manifolds:

$$\beta_{\mathrm{i}} = \frac{2\,\Delta p_{\mathrm{i}}}{\rho\,\bar{v}_{\mathrm{i}}^{2}}\,, \qquad \beta_{\mathrm{o}} = \frac{2\,\Delta p_{\mathrm{o}}}{\rho\,\bar{v}_{\mathrm{o}}^{2}}\,. \tag{34}$$

Figure 24 reports the β_{i} and β_{o} values as a function of $\mathrm{Re}_{\mathrm{D_p}}$: At low Reynolds values, which correspond to the inner flows of oil coolers, the loss coefficients decrease with increasing $\mathrm{Re}_{\mathrm{D_p}}$ and cooler thickness S. On the other hand, at high Re-values, which correspond to the flow rates of the water radiators and charge air coolers, both concentrated loss coefficients remain almost unchanged, with varying $\mathrm{Re}_{\mathrm{D_p}}$ and S.

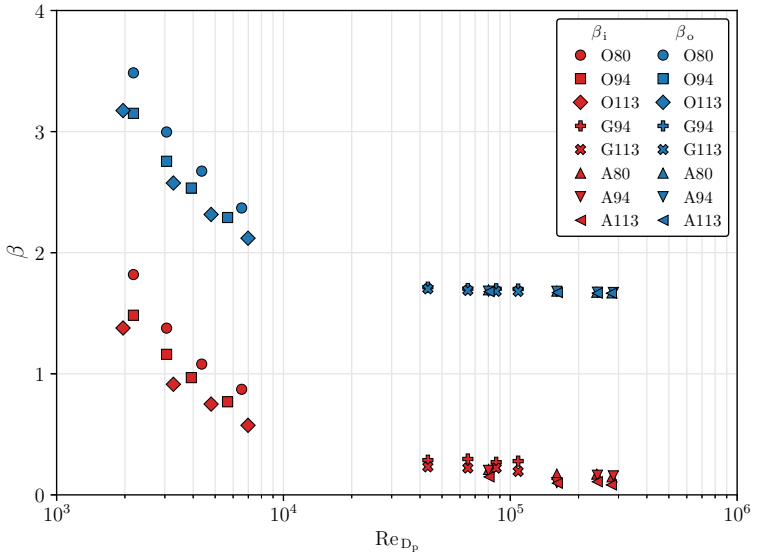


Figure 24. Global head losses model: Concentrated loss coefficients of the inlet (red) and outlet (blue) manifolds.

The values of the concentrated loss coefficients are used to derive suitable correlations by following an analogous approach to the one employed in [42]:

$$\beta = k_1 \, \mathrm{Re}^{k_2} + k_3 \, , \tag{35}$$

where the coefficients k_i are computed by combining the ratio between the thickness of the manifolds, S, and the diameter of their inlet and outlet pipes, D_p, with the q_{ij} values reported in Table 9.

$$k_i = q_{i1} \left(\frac{S}{D_\mathrm{p}} \right)^{q_{i2}} \tag{36}$$

Table 9. Values of q_{ij} coefficients in Equation (36).

Coefficient	q_{11}	q_{12}	q_{21}	q_{22}	q_{31}	q_{320}
β_i	2385	−1.580	−0.826	−0.076	0.196	−0.509
β_o	272.2	1.791	−0.621	0.375	1.602	0.022

3.4. Global Models

3.4.1. Heat Transfer

Figure 25 shows the comparison between the experimentally obtained heat transfer rates and the numerical results from the global model for heat transfer, as described in Section 2.5.1. The remarkable agreement between the numerical and experimental data found for charge air coolers (Figure 25f–h) demonstrates the validity of the selected modelling approach. Greater maximum deviations of ±10% and ±20% are found for water radiators and oil coolers, respectively. O94 features the highest deviations, reaching ±38%. These deviations can be traced back to the fact that the models developed in this work are derived purely from nominal geometric data, physical principles, and established models. On the other hand, possible fouling or shape imperfections are not taken into account.

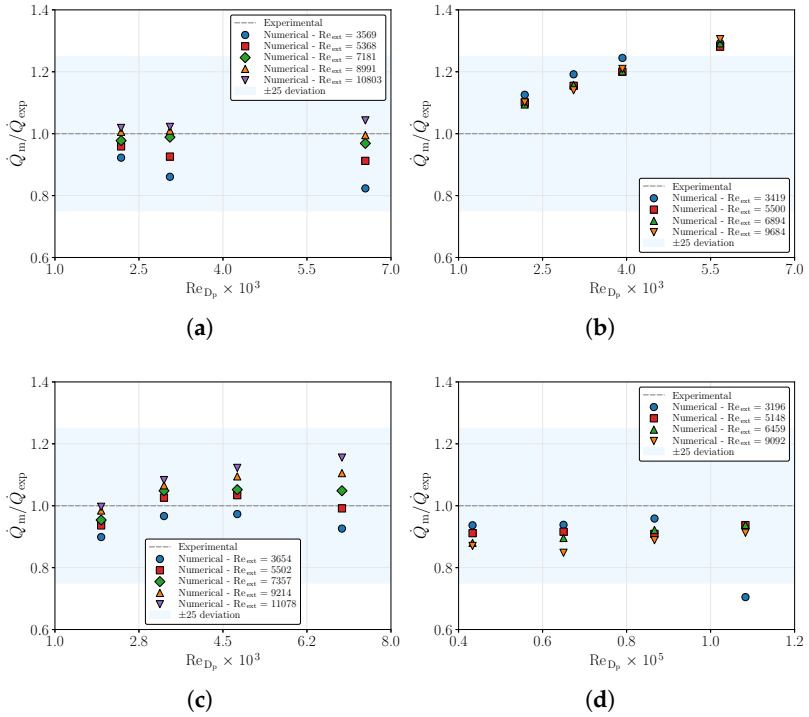


Figure 25. *Cont.*

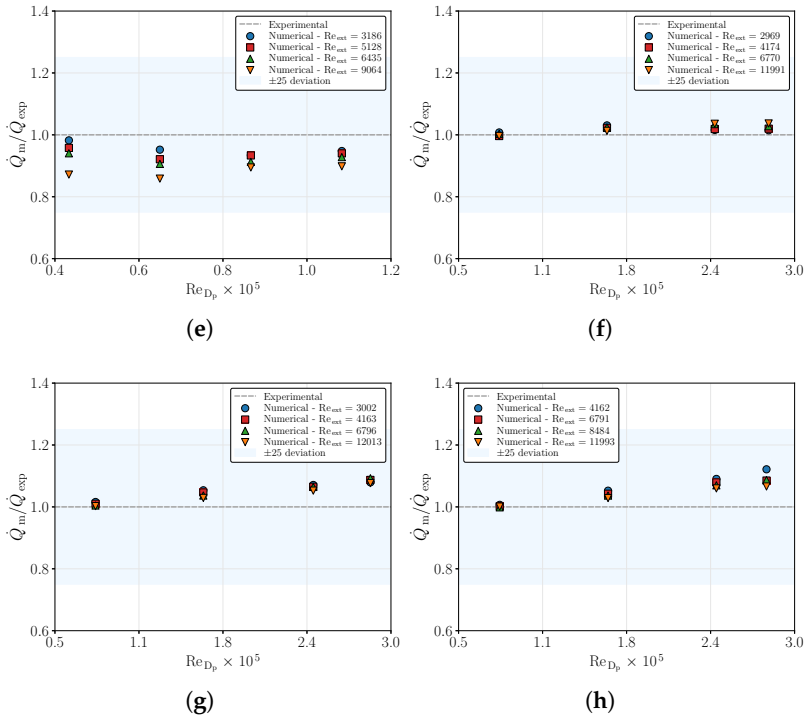


Figure 25. Global thermal model: Comparison between the numerical results and available experimental data for O80 (**a**), 094 (**b**), 0113 (**c**), G94 (**d**), G113 (**e**), A80 (**f**), A94 (**g**), and A113 (**h**) coolers.

3.4.2. Internal Head Losses

The internal head losses, computed according to the approach presented in Section 2.5.2, are compared with the available experimental data in Figure 26. The results related to oil coolers and water radiators are remarkably accurate as, for the majority of the flow rates tested, the difference between the numerical and experimental results is less than ±10%. On average, the results on charge air coolers are much less accurate, as in the majority of the tested cases the deviation between the numerical and experimental results is close to +20%; moreover, there are two outliers which show deviations of +120% and +185%. The higher deviations found in the analyses of charge air coolers suggest that the proposed methodology may have some limitations, which could be addressed by performing CFD analyses of the complete heat exchangers, including the computation of the temperature field, along with an ideal gas model for the working fluid. This approach could lead to more accurate results, but at the cost of much greater computational effort and complexity.

Figure 27 shows the values of pressure drop associated with the inlet and outlet manifolds, and the internal channels expressed as a fraction of the total head losses. In the case of oil coolers ($2000 \leq \mathrm{Re}_{D_p} \leq 7000$), the major contribution to the total losses is given by the internal channels, while both manifolds play a minor role. As the Reynolds number increases, the contribution of the outlet manifold increases dramatically until it becomes the main cause of head losses for water radiators and charge air coolers. Conversely, the contribution of internal channels decreases until it becomes of the same order of magnitude as the one of the inlet manifold, which slightly grows with increasing Re_{D_p}. As the thickness of the heat exchanger, S, increases, the contribution of the outlet manifold grows, resulting in a corresponding decrease in the contribution of the internal channels. Meanwhile, the relative loss associated with the inlet manifold remains almost unchanged with varying S. Similarly, it can also be noted that the large fluid density variation in charge air coolers tends to increase the contribution of the outlet manifold at the expense of the

internal channels one. The relative loss of the inlet manifold is less affected by the large temperature difference.

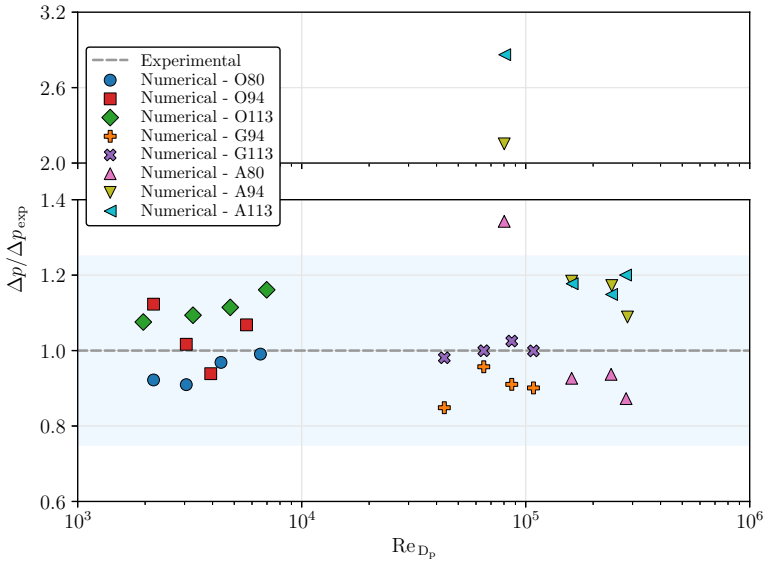


Figure 26. Global head losses model, internal flow: Comparison between the numerical results and available experimental data for all the considered heat exchangers.

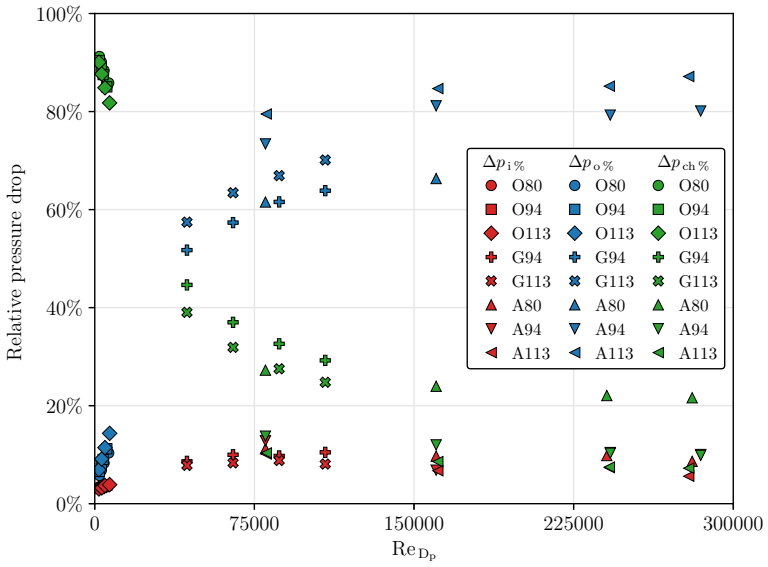


Figure 27. Global head losses model, internal flow: Relative pressure drops of the inlet manifold (red), the outlet manifold (blue), and the internal channels (green).

These results underline the importance of considering the head losses of the manifolds when carrying out optimizations on complete heat exchangers, as these losses alter the relative weight between the heat transfer effectiveness and head losses in the internal channels. For instance, in charge air coolers, optimising the geometry of the internal fins to reduce head losses of the core at the expense of heat transfer effectiveness may not be advantageous, given that roughly 90% of the total head losses are given by the manifolds.

3.5. External Head Losses

Figure 28 shows the comparison between the numerical values of external head losses and the experimental ones. For most of the tested cases, the deviation between the numerical and experimental results is less than ±25%. Furthermore, many of the

heat exchangers considered feature an average deviation of ±10% across the tested flow rates. The greater uncertainties observed in some cases may be due to the fact that, in the experimental test bed, the outlet of the external side of the heat exchangers is in free air, as seen in Figure 8a. This can lead to uncertainties in the measurement of the outlet air temperature and pressure. Overall, these results confirm the validity of the proposed approach.

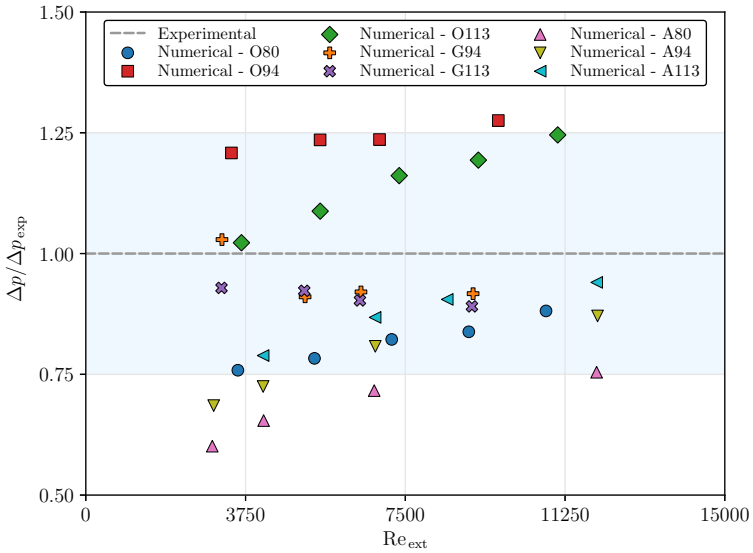


Figure 28. Global head losses model, external flow: Comparison between the numerical results and available experimental data for all heat exchangers considered.

4. Concluding Remarks

In this work, an original multiscale modelling approach for plate-fin heat exchangers was developed purely on the basis of nominal geometric parameters, physical principles, and established models. The finned surfaces and the inlet and outlet manifolds were analysed by means of dedicated CFD models, while the overall thermo-hydraulic performance of the heat exchangers was evaluated by means of global models based on the $\varepsilon - \mathrm{NTU}$ approach and the Darcy–Weisbach formula, where the coefficients were derived from numerical results.

Numerical results on extended surfaces were compared with selected correlations from the literature, showing that, although quite a large amount of data is available on these fin geometries, dedicated numerical analyses are still necessary to obtain accurate results for the fin configurations used in actual industrial applications. The presented approach was validated by comparing numerical results from the overall models with the available experimental data, showing a remarkable agreement. In addition, the comparison between the sources of internal head losses showed that in oil coolers, which typically operate at low values of Reynolds number, almost all the losses are due to the internal channels. Conversely, in water radiators and charge air coolers, which typically operate at high Reynolds number values, 90% of the total losses are given by the manifolds, underlining the importance of considering this contribution during the verification and optimisation procedures of these types of coolers.

The approach presented in this work, which can be practically applied to heat exchangers of any architecture, is an improvement over common modelling techniques, as it retains the simplicity of a global modelling procedure while achieving levels of accuracy which are typical of higher-order methods. Future research efforts will be directed towards the use of the modelling approach proposed in this work to carry out optimisation procedures on complete heat exchangers using generalised response surfaces for the evaluation of the thermo-hydraulic performance of finned channels, such as those developed in [33].

Author Contributions: Conceptualization, D.A., A.L. and M.G.; methodology, A.L., D.A. and M.G.; software, A.L. and M.G.; validation, M.G. and A.L.; formal analysis, M.G. and A.L.; investigation, M.G. and A.L.; resources, D.A.; data curation, M.G. and L.C.; writing—original draft preparation, M.G. and L.C.; writing—review and editing, M.G., D.A. and M.C.; visualization, M.G.; supervision, D.A. and M.C.; project administration, D.A.; funding acquisition, D.A. All authors have read and agreed to the published version of the manuscript.

Funding: This research received no external funding.

Data Availability Statement: The data that have been used are confidential.

Acknowledgments: The authors would like to thank Hugo Lepine and Valentin Grienenberger from ISAE-ENSMA—École Nationale Supérieure de Mécanique et d'Aérotechnique, Poitiers, France, for the excellent work done during their internship, which contributed to a significant portion of the numerical results presented in this work.

Conflicts of Interest: The authors declare the following financial interests/personal relationships which may be considered as potential competing interests: Diego Angeli reports a relationship with VEMA Industries S.r.l. that includes funding grants. Luigi Calò reports a relationship with VEMA Industries S.r.l. that includes employment. All other authors declare that they have no known competing financial interests or personal relationships that could have appeared to influence the work reported in this paper.

Nomenclature

The following abbreviations are used in this manuscript:

Latin letters

a	wave amplitude [m]
A	area [m^2]
b_i	coefficients in Equation (19)
c_i	coefficients in Equation (20)
c_p	specific heat [$J\,kg^{-1}\,K^{-1}$]
C	heat capacity rate [$W\,K^{-1}$]
d_{kr}	coefficients in Equation (32)
D_h	hydraulic diameter [m]
e_{kr}	coefficients in Equation (33)
f	equivalent Darcy friction factor [−]
H	heat exchanger height [m]
j	Colburn factor [−]
k_n	coefficients in Equation (35)
l	offset length and half the wavelength [m]
L	heat exchanger core length [m]
L_e	effective wavy-fin length [m]
$\vec{n}$	normal unit vector [−]
N_{ch}	number of internal channels [−]
Nu	Nusselt number [−]
NTU	number of transfer units [−]
p	fluid pressure [Pa]
P	wetted perimeter [m]
Pr	Prandtl number [−]
q_{ij}	coefficients in Equation (36)
$\vec{q}$	heat flux [$W\,m^{-2}$]
$\dot{Q}$	heat [W]
R	thermal resistance [$K\,W^{-1}$]
Re	Reynolds number [−]
S	heat exchanger thickness [m]

t	fin thickness [m]
T	temperature [K]
U	overall heat transfer coefficient [W m^{-2} K^{-1}]
$\vec{v}$	fluid velocity [m s^{-1}]
W	manifold width [m]
x	fin pitch [m]
y	fin height [m]
Greek letters	
β	concentrated loss coefficient [−]
ε	effectiveness [−]
ϑ	dimensionless temperature [−]
λ	thermal conductivity [W m^{-1} K^{-1}]
μ	dynamic viscosity [Pa s]
ν	kinematic viscosity [m^2 s^{-1}]
ρ	density [kg m^{-3}]
σ_m	momentum sink [m s^{-2}]
Φ	relative friction factor in the entrance region [−]
χ	single-fin module number [−]
Ψ	relative Nusselt number in the entrance region [−]
Subscripts	
b	bulk
ch	channel
e	entrance
exp	experimental
ext	external
F	Fanning
fd	fully developed
i	inlet
int	internal
m	model
o	outlet
s	solid
t	turbulent
w	wall
Superscripts	
*	dimensionless

References

1. Kays, W.M.; London, A.L. *Compact Heat Exchangers*, 3rd ed.; McGraw-Hill: New York, NY, USA, 1984.
2. London, A.L.; Shah, R.K. Offset Rectangular Plate-Fin Surfaces Heat Transfer and Flow Friction Characteristics. *J. Eng. Power* **1968**, *90*, 218–228. [CrossRef]
3. Wieting, A.R. Empirical Correlations for Heat Transfer and Flow Friction Characteristics of Rectangular Offset-Fin Plate-Fin Heat Exchangers. *J. Heat Transf.* **1975**, *97*, 488–490. [CrossRef]
4. Mochizuki, S.; Yagi, Y.; Yang, W.-J. Transport phenomena in stacks of interrupted parallel-plate surfaces. *Exp. Heat Transf.* **1987**, *1*, 127–140. [CrossRef]
5. Manglik, R.M.; Bergles, A.E. Heat transfer and pressure drop correlations for the rectangular offset strip fin compact heat exchanger. *Exp. Therm. Fluid Sci.* **1995**, *10*, 171–180. [CrossRef]
6. Dubrovsky, E.V.; Vasiliev, V.Y. Enhancement of convective heat transfer in rectangular ducts of interrupted surfaces. *Int. J. Heat Mass Transf.* **1988**, *31*, 807–818. [CrossRef]
7. Joshi, H.M.; Webb, R.L. Heat transfer and friction in the offset stripfin heat exchanger. *Int. J. Heat Mass Transf.* **1987**, *30*, 69–84. [CrossRef]
8. Yang, Y.; Li, Y. General prediction of the thermal hydraulic performance for plate-fin heat exchanger with offset strip fins. *Int. J. Heat Mass Transf.* **2014**, *78*, 860–870. [CrossRef]

9. Wen, J.; Yang, H.; Tong, X.; Li, K.; Wang, S.; Li, Y. Optimization investigation on configuration parameters of serrated fin in plate-fin heat exchanger using genetic algorithm. *Int. J. Therm. Sci.* **2016**, *101*, 116–125. [CrossRef]
10. Zheng, X.; Qi, Z. A comprehensive review of offset strip fin and its applications. *Appl. Therm. Eng.* **2018**, *139*, 61–75. [CrossRef]
11. Li, L.; Lu, J.; Fang, H.; Yin, Z.; Wang, T.; Wang, R.; Fan, X.; Zhao, L.; Tan, D.; Wan, Y. Lattice Boltzmann Method for Fluid-Thermal Systems: Status, Hotspots, Trends and Outlook. *IEEE Access* **2020**, *8*, 27649–27675. [CrossRef]
12. Kim, M.S.; Lee, J.; Yook, S.J.; Lee, K.S. Correlations and optimization of a heat exchanger with offset-strip fins. *Int. J. Heat Mass Transf.* **2011**, *54*, 2073–2079. [CrossRef]
13. Dong, J.; Chen, J.; Zhang, W.; Hu, J. Experimental and numerical investigation of thermal -hydraulic performance in wavy fin-and-flat tube heat exchangers. *Appl. Therm. Eng.* **2010**, *30*, 1377–1386. [CrossRef]
14. Manglik, R.M.; Zhang, J.; Muley, A. Low Reynolds number forced convection in three-dimensional wavy-plate-fin compact channels: Fin density effects. *Int. J. Heat Mass Transf.* **2005**, *48*, 1439–1449. [CrossRef]
15. Goldstein, L., Jr.; Sparrow, E.M. Heat/Mass Transfer Characteristics for Flow in a Corrugated Wall Channel. *J. Heat Transf.* **1977**, *99*, 187–195. [CrossRef]
16. Rush, T.A.; Newell, T.; Jacobi, A.M. An experimental study of flow and heat transfer in sinusoidal wavy passages. *Int. J. Heat Mass Transf.* **1999**, *42*, 1541–1553. [CrossRef]
17. Dong, J.; Chen, J.; Chen, Z.; Zhou, Y.; Zhang, W. Heat transfer and pressure drop correlations for the wavy fin and flat tube heat exchangers. *Appl. Therm. Eng.* **2007**, *27*, 2066–2073. [CrossRef]
18. Asako, Y.; Faghri, M. Finite-Volume Solutions for Laminar Flow and Heat Transfer in a Corrugated Duct. *J. Heat Transf.* **1987**, *109*, 627–634. [CrossRef]
19. Zhang, J.; Kundu, J.; Manglik, R.M. Effect of fin waviness and spacing on the lateral vortex structure and laminar heat transfer in wavy-plate-fin cores. *Int. J. Heat Mass Transf.* **2004**, *47*, 1719–1730. [CrossRef]
20. Metwally, H.; Manglik, R.M. Enhanced heat transfer due to curvature-induced lateral vortices in laminar flows in sinusoidal corrugated-plate channels. *Int. J. Heat Mass Transf.* **2004**, *47*, 2283–2292. [CrossRef]
21. Aliabadi, M.K.; Hormozi, F.; Rad, E.H. New correlations for wavy plate-fin heat exchangers: Different working fluids. *Int. J. Numer. Methods Heat Fluid Flow* **2012**, *24*, 1086–1108. [CrossRef]
22. Tao, Y.B.; He, Y.L.; Wu, Z.G.; Tao, W.Q. Numerical Design of an Efficient Wavy Fin Surface Based on the Local Heat Transfer Coefficient Study. *J. Enhanc. Heat Transf.* **2007**, *14*, 315–332. [CrossRef]
23. Pham, M.V.; Plourde, F.; Doan, S.K. Turbulent heat and mass transfer in sinusoidal wavy channels. *Int. J. Heat Fluid Flow* **2008**, *29*, 1240–1257. [CrossRef]
24. de Vasconcelos Segundo, E.H.; Mariani, V.C.; dos Santos Coelho, L. Design of heat exchangers using Falcon Optimization Algorithm. *Appl. Therm. Eng.* **2019**, *156*, 119–144. [CrossRef]
25. Zarea, H.; Kashkooli, F.M.; Mehryan, A.M.; Saffarian, M.R.; Beherghani, E.N. Optimal design of plate-fin heat exchangers by a Bees Algorithm. *Appl. Therm. Eng.* **2014**, *69*, 267–277. [CrossRef]
26. Yousefi, M.; Enayatifar, R.; Darus, A. Optimal design of plate-fin heat exchangers by a hybrid evolutionary algorithm. *Int. Commun. Heat Mass Transf.* **2012**, *39*, 258–263. [CrossRef]
27. Yousefi, M.; Enayatifar, R.; Darus, A.; Abdullah, A. Optimization of plate-fin heat exchangers by an improved harmony search algorithm. *Appl. Therm. Eng.* **2013**, *50*, 877–885. [CrossRef]
28. Hao, J.H.; Chen, Q.; Ren, J.X.; Zhang, M.Q.; Ai, J. An experimental study on the offset-strip fin geometry optimization of a plate-fin heat exchanger based on the heat current model. *Appl. Therm. Eng.* **2019**, *154*, 111–119. [CrossRef]
29. Hao, J.; Chen, Q.; Li, X.; Zhao, T. A Correction Factor-Based General Thermal Resistance Formula for Heat Exchanger Design and Performance Analysis. *J. Therm. Sci.* **2021**, *30*, 892–901. [CrossRef]
30. Chen, Q.; Hao, J.H.; Zhao, T. An alternative energy flow model for analysis and optimization of heat transfer systems. *Int. J. Heat Mass Transf.* **2017**, *108*, 712–720. [CrossRef]
31. Zhang, M.Q.; Chen, Q.; Shao, W.; Chen, X.; Hao, J.H. An integral identification method of characteristic parameters and optimization of parallel connection heat transfer systems based on the power flow method. *Appl. Therm. Eng.* **2018**, *143*, 1057–1067. [CrossRef]
32. Awad, M.; Muzychka, Y.S. Models for pressure drop and heat transfer in air cooled compact wavy fin heat exchangers. *J. Enhanc. Heat Transf.* **2011**, *18*, 191–207. [CrossRef]
33. Grespan, M.; Calò, L.; Carlesso, L.; Leonforte, A.; Angeli, D. A comprehensive numerical study on heat transfer and friction characteristics of offset-strip fins. *Appl. Therm. Eng.* **2024**, *256*, 124083. [CrossRef]
34. Weller, H.G.; Tabor, G.; Jasak, H.; Fureby, C. A tensorial approach to computational continuum mechanics using object-oriented techniques. *Comput. Phys.* **1998**, *12*, 620–631. [CrossRef]
35. Patankar, S.; Spalding, D. Paper 5—A calculation procedure for heat, mass and momentum transfer in three-dimensional parabolic flows. In *Numerical Prediction of Flow, Heat Transfer, Turbulence and Combustion*; Patankar, S.V., Pollard, A., Singhal, A.K., Vanka, S.P., Eds.; Pergamon: Oxford, UK, 1983; pp. 54–73. [CrossRef]

36. Menter, F. Two-equation eddy-viscosity turbulence models for engineering applications. *AIAA J.* **1994**, *32*, 1598–1605. [CrossRef]
37. Forchheimer, P. Wasserbewegung durch boden. *Z. Ver. Dtsch. Ing.* **1901**, *45*, 1782–1788.
38. Marquardt, D. An Algorithm for Least-Squares Estimation of Nonlinear Parameters. *J. Soc. Ind. Appl. Math.* **1963**, *11*, 431–441. [CrossRef]
39. Thomas, P.; Middlecoff, J. Direct control of the grid point distribution in meshes generated by elliptic equations. *AIAA J.* **1980**, *18*, 652–656. [CrossRef]
40. Crameri, F. Scientific Colour Maps. 2023. Available online: https://zenodo.org/records/8035877 (accessed on 16 January 2025).
41. Virtanen, P.; Gommers, R.; Oliphant, T.E.; Haberland, M.; Reddy, T.; Cournapeau, D.; Burovski, E.; Peterson, P.; Weckesser, W.; Bright, J.; et al. SciPy 1.0: Fundamental Algorithms for Scientific Computing in Python. *Nat. Methods* **2020**, *17*, 261–272. [CrossRef] [PubMed]
42. Grespan, M.; Leonforte, A.; Cavazzuti, M.; Calo, L.; Angeli, D. Accurate reduced-order modelling of plate-fin heat exchangers. In *Proceedings of the IHTC Digital Library*; Begel House Inc.: Danbury, CT, USA, 2023.

Disclaimer/Publisher's Note: The statements, opinions and data contained in all publications are solely those of the individual author(s) and contributor(s) and not of MDPI and/or the editor(s). MDPI and/or the editor(s) disclaim responsibility for any injury to people or property resulting from any ideas, methods, instructions or products referred to in the content.